

ATMOSPHERIC SCIENCE

Rapid growth of anthropogenic organic nanoparticles greatly alters cloud life cycle in the Amazon rainforest

Rahul A. Zaveri^{1*}, Jian Wang², Jiwen Fan¹, Yuwei Zhang¹, John E. Shilling¹, Alla Zelenyuk¹, Fan Mei¹, Rob Newsom¹, Mikhail Pekour¹, Jason Tomlinson¹, Jennifer M. Comstock¹, Manish Shrivastava¹, Edward Fortner³, Luiz A. T. Machado⁴, Paulo Artaxo⁵, Scot T. Martin⁶

Aerosol-cloud interactions remain uncertain in assessing climate change. While anthropogenic activities produce copious aerosol nanoparticles smaller than 10 nanometers, they are too small to act as efficient cloud condensation nuclei (CCN). The mechanisms responsible for particle growth to CCN-relevant sizes are poorly understood. Here, we present aircraft observations of rapid growth of anthropogenic nanoparticles downwind of an isolated metropolis in the Amazon rainforest. Model analysis reveals that the sustained particle growth to CCN sizes is predominantly caused by particle-phase diffusion-limited partitioning of semivolatile oxidation products of biogenic hydrocarbons. Cloud-resolving numerical simulations show that the enhanced CCN concentrations in the urban plume substantially alter the formation of shallow convective clouds, suppress precipitation, and enhance the transition to deep convective clouds. The proposed nanoparticle growth mechanism, expressly enabled by the abundantly formed semivolatile organics, suggests an appreciable impact of anthropogenic aerosols on cloud life cycle in previously unpolluted forests of the world.

INTRODUCTION

Atmospheric aerosols modulate Earth's energy balance by directly scattering incoming solar radiation and indirectly by forming clouds that reflect more radiation back to space (1). The marked increase in the global aerosol concentrations resulting from anthropogenic activities during the industrial age has perturbed this energy balance by partially offsetting the warming caused by the concomitant increase in greenhouse gases, but the extent of the influence of anthropogenic aerosols on climate change remains uncertain (2–4). Depending on their composition, aerosols larger than about 40 to 50 nm in diameter can efficiently serve as cloud condensation nuclei (CCN) upon which liquid water can condense to form shallow, warm clouds. Higher concentrations of CCN due to anthropogenic emissions thus lead to higher concentrations of smaller cloud droplets that not only scatter more light (5) but also suppress rain formation from shallow convection, extend cloud lifetime, and thereby reflect even more solar radiation (6, 7).

However, most anthropogenic aerosols originate as nanoparticles smaller than 10 nm, which are too small to be climatically active. For example, large amounts of nanoparticles are directly emitted from widespread sources such as oil and natural gas-fired power plants (8, 9) and vehicular traffic (10). Another notable source is the nucleation of sulfuric acid vapors formed from oxidation of sulfur dioxide—a by-product emitted from oil refineries and coal-fired power plants (11). The climate impact of these nanoparticles strongly depends on their ability to rapidly grow to CCN-relevant sizes by condensation of vapors in competition to loss by coagulation with larger preexisting aerosols.

Growth of nanoparticles is largely controlled by condensation of atmospheric organic vapors (12). Nonmethane volatile organic

compounds (VOCs) emitted from both anthropogenic and biogenic sources undergo gas-phase oxidation to form myriad products with a range of volatilities [i.e., effective saturation concentration (C^*)]. Compounds with sufficiently low volatility may nucleate to form new particles or partition into the preexisting particle phase to form secondary organic aerosol (SOA), which constitutes a major fraction of the submicron atmospheric aerosols (13, 14). Overall SOA yields and size-dependent particle growth mechanisms strongly depend on the volatility of the condensing products and their multiphase reactions to form nonvolatile compounds (15–18). Oxidation of biogenic VOCs such as monoterpenes produces extremely low-volatility compounds (ELVOCs) ($C^* < 10^{-4} \mu\text{g m}^{-3}$) that condense effectively irreversibly to preexisting aerosol (19, 20). ELVOCs are necessary for the initial growth of the smallest nanoparticles because their low vapor pressure helps overcome the Kelvin effect, which enhances the volatility of molecules over a curved surface compared to that over a flat surface (21). In comparison, oxidation of isoprene (the most abundantly emitted biogenic nonmethane VOC) and anthropogenic VOCs produce substantial amounts of semivolatile organic compounds (SVOCs) (22–24) with C^* between about 0.1 and $100 \mu\text{g m}^{-3}$. SVOCs can reversibly partition between the gas and particle phases and are traditionally assumed to favor the growth of large preexisting organic particles via equilibrium partitioning (25).

Rapid gas-particle equilibrium is achieved when the particles are liquid-like [i.e., particle-phase bulk diffusivity (D_b) $> 10^{-10} \text{cm}^2 \text{s}^{-1}$] (18, 26). However, mounting evidence indicates that aged SOA particles are, in many cases, viscous semisolids under low to fairly high relative humidity (RH) conditions (27–35). The presence of primary organic species such as polycyclic aromatic hydrocarbons in SOA also substantially increases the viscosity and decreases the volatility of the mixed organic particles (28, 36). In the case of such semisolid particles, mass transfer of SVOCs involves slow bulk diffusion ($D_b < 10^{-14} \text{cm}^2 \text{s}^{-1}$) that can greatly prolong the gas-particle equilibration time scale (18, 26), and the resulting partitioning may not be consistent with the instantaneous equilibrium assumption (37). Because the bulk diffusion time scale varies as the square of particle

Copyright © 2022
The Authors, some
rights reserved;
exclusive licensee
American Association
for the Advancement
of Science. No claim to
original U.S. Government
Works. Distributed
under a Creative
Commons Attribution
NonCommercial
License 4.0 (CC BY-NC).

Downloaded from <https://www.science.org> on January 24, 2022

¹Pacific Northwest National Laboratory, Richland, WA 99352, USA. ²Washington University in Saint Louis, Saint Louis, MO 63130, USA. ³Aerodyne Research, Inc., Billerica, MA 01821, USA. ⁴National Institute for Space Research, São José dos Campos, São Paulo 12227-010, Brazil. ⁵Institute of Physics, University of São Paulo, São Paulo 05508-090, Brazil. ⁶Harvard University, Cambridge, MA 02138, USA.
*Corresponding author. Email: rahul.zaveri@pnnl.gov

diameter, small particles reach equilibrium much faster than the larger ones. Consequently, hindered partitioning of SVOCs into large semisolid particles causes SVOCs to remain longer in the gas phase and thereby become available for preferential growth of nanoparticles, especially when the SVOCs undergo particle-phase accretion reactions to form effectively nonvolatile oligomers (33, 34, 38). A bulk diffusion-limited dynamic SOA partitioning mechanism was recently suggested for aerosol growth observed in laboratory chamber experiments (33, 34, 39) and oxidation flow reactor studies on atmospheric aerosol samples (40). Here, we present evidence for such a growth mechanism occurring under ambient conditions during the Green Ocean Amazon (GoAmazon2014/5) field campaign in Brazil.

The GoAmazon2014/15 campaign (41) was centered on Manaus, an isolated metropolis in the central Amazon Basin with a population of over 2 million people. A mix of several diesel, fuel oil, and natural gas power plants; a refinery; vehicular traffic in the city; and large oceangoing ships are a substantial source of pollutant trace gases (42) and aerosols (43, 44), including copious amounts of nanoparticles from new particle formation facilitated by interactions between urban pollution and biogenic VOCs (45). During the wet season, the ambient conditions in the surrounding rainforest resemble those of the preindustrial era in which the CCN are naturally produced via biogenic SOA formation (46), with isoprene being the dominant precursor VOC (47). The impact of the anthropogenic aerosols, especially the nanoparticles, on clouds and precipitation in this otherwise pristine region may depend on their ability to grow to CCN active sizes via SOA formation from a mix of both biogenic and anthropogenic VOCs. As part of the campaign, the U.S. Department of Energy's Gulfstream 1 (G-1) research aircraft made semi-Lagrangian measurements of aerosols and trace gases over and downwind of Manaus (see the "G-1 aircraft measurements" section). We examine two observational episodes of the Manaus urban plume evolution. The first episode on the morning of 13 March 2014, one of the exemplary days with few clouds in the area during the wet season (48), is selected to investigate the mechanism responsible for the rapid growth of nanoparticles observed in the urban plume. On the morning of 13 March, the Manaus region happened to be in the subsidence branch between two intense storms, which brought down dry and cool air that is unfavorable for cumulus cloud formation. This clear-air episode facilitates the model interpretation of aircraft measurements by avoiding the overly complex effects of clouds and precipitation that otherwise usually occur in the area. The second episode on the afternoon of 17 March 2014 is selected to investigate a possible effect of the grown nanoparticles on clouds and precipitation as the meteorological conditions in the urban plume in this episode transitioned from shallow cumulus to deeper, precipitating cloud (49).

RESULTS AND DISCUSSION

Aircraft observations of anthropogenic nanoparticle growth

Air pollutants from Manaus were advected westward on the morning of 13 March 2014. A Lagrangian observational strategy to characterize their temporal evolution would have entailed repeated sampling in the same air parcel as it was advected downwind. However, such observations are difficult to obtain in practice. Instead, a semi-Lagrangian strategy was used in which the G-1 made four cross-wind transects at an altitude of 472 ± 14 m above mean sea level (MSL) at increasing downwind distances from the city between

10:36 and 11:36 local standard time (LST) (Fig. 1A). The polluted air parcels in these transects passed over Manaus at different times. On the basis of the mean wind speed of 7.3 ± 1.4 m s⁻¹ in the plume, the ages (Δt) of the second, third, and fourth transects relative to the position of the first transect were estimated at about 51 ± 4 , 102 ± 9 , and 165 ± 14 min, respectively. Thus, in the Lagrangian frame of reference, the urban air parcels observed in the fourth transect would have been at the location of the first transect at approximately 8:40 LST. The ambient air temperature and RH in the plume were about 299 K and 80%, respectively. Observations at the T3 ground site between 8:40 and 11:24 LST indicate that plume area remained largely cloud-free, with a mean total sky cloud cover of $20 \pm 11.6\%$ and no rain clouds; the shortwave downwelling irradiance increased from 770 to 1300 W m⁻² and the surface temperature rose by 3.4 K, while the RH decreased from about 84 to 70% (fig. S1).

The total aerosol (larger than 3 nm in diameter) number concentration (N_{tot}) observed along the aircraft flight path illustrates the urban plume footprint, with the concentration peaks in each transect denoted as P1 to P4 (Fig. 1A). The average N_{tot} was 616 ± 99 cm⁻³ in the background air (denoted as B). In comparison, N_{tot} in the urban plume was greater than 30,000 cm⁻³ in the first transect at P1 (closest to Manaus), with about 8100 cm⁻³ being smaller than 10 nm (fig. S2), where the plume was as wide as the diameter of the city. The plume broadened with increasing downwind distance due to dispersion and appears to have doubled its width in the fourth transect where N_{tot} decreased to ~ 5000 cm⁻³ (at P4). As the plume was advected up to the fourth transect, the mixed boundary layer (BL) height grew from about 648 to 1098 m (see the "BL height estimation using Doppler lidar" section and fig. S3). The horizontal dispersion and vertical mixing in the growing BL together yield an overall first-order dilution rate of $\lambda = 7.4 \times 10^{-3}$ min⁻¹ (see the "Plume dilution rate estimation" section). Along with N_{tot} , carbon monoxide (CO) mixing ratios as well as particulate organics, sulfate, and nitrate mass concentrations were also enhanced in the urban plume (Fig. 1B). Organics constituted about 80 to 85% of the total submicron aerosol mass in each plume transect (44). Sulfate concentrations peaked in the southern portion of the plume, consistent with its origin from the refinery located at the south end of Manaus (fig. S2). In contrast, the peak organic and nitrate concentrations occurred in the center of the plume and coincided with the peak N_{tot} (fig. S2). Because CO is effectively chemically inert on the time scales considered here, its mixing ratio should have progressively decreased downwind due to dilution. However, it remained around 120 parts per billion by volume (ppbv) and even increased to 140 ppbv at P3, indicating that CO emissions were not uniform in time, with the high mixing ratio at P3 traced back to rush hour traffic in Manaus around 8:00 LST (48). In stark contrast, the progressive decrease in N_{tot} downwind can be largely explained by dilution alone as $N_{\text{dil}} = N_{\text{P1}} \times \exp(-\lambda \Delta t)$, with the remaining loss attributed to coagulation (Fig. 2A). Here, Δt is the relative plume age with respect to the plume location P1. This result suggests that there was a nearly steady source of nanoparticles in Manaus that was largely independent of the rush hour, such as organic-mediated new particle formation over the urban area (45) as well as emissions from the oil and natural gas-fired power plants, and supports the Lagrangian model analysis of the plume presented shortly.

Figure 1 (C and D) shows the evolution of aerosol number and volume size distributions (1-min average) at the plume peaks marked in Fig. 1B. There was a clear enhancement of the Aitken mode

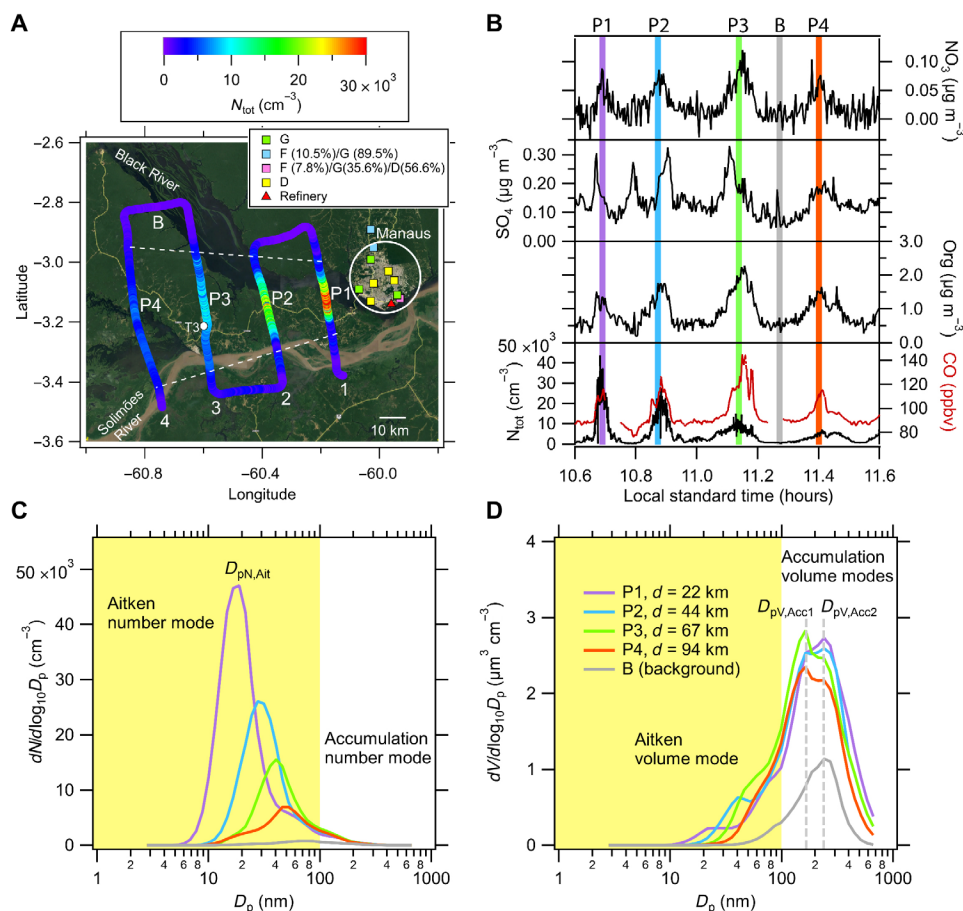


Fig. 1. Manaus urban plume on 13 March 2014 between 10:36 and 11:36 LST. (A) Total aerosol number concentration (N_{tot}) along the G-1 aircraft flight path consisting of four downwind transects at an altitude of 472 ± 14 m MSL at increasing distances from the center of Manaus. Red triangle indicates the location of an oil refinery, and squares indicate the locations of power plants, with fuel types denoted as G for natural gas, F for fuel oil, and D for diesel. Plume peaks are denoted as P1 to P4, and background air sample denoted as B. Dotted lines approximately demarcate the width of the plume. T3 indicates the location of a ground measurement site. (B) Time series of N_{tot} along with key aerosol species mass concentrations. Vertical colored bands denote 1-min periods centered at the plume peaks and background sample. (C) Evolution of aerosol number size distribution (1-min average) along the plume peaks and in background air sample. (D) Evolution of aerosol volume size distribution. Yellow and white areas represent the Aitken and accumulation modes, respectively.

(20 to 100 nm) aerosol number concentrations and accumulation mode (100 to 2500 nm) aerosol volume concentrations in the plume relative to the background. While the sizes, compositions, and phase states of the newly formed and the directly emitted nanoparticles may have been different at their originations, the Aitken mode at P1 had grown to about 19 nm and did not show any signs of double peaks, suggesting that its composition was rather uniform and likely dominated by freshly formed SOA. The Aitken mode number diameter ($D_{\text{pN,Ait}}$) rapidly increased from ~ 19 nm at P1 to ~ 50 nm at P4 with an average growth rate of about 11 nm hour^{-1} as N_{tot} decreased due to dilution and coagulation. In contrast, the accumulation mode volume size distribution consisted of two submodes with volume diameters $D_{\text{pV,Acc1}} = 164$ nm and $D_{\text{pV,Acc2}} = 241$ nm, which remained constant throughout the plume, with the smaller accumulation volume mode (“Acc1”) peak height becoming more pronounced with aging, while the larger accumulation volume mode (“Acc2”) decreased with aging (Fig. 1D). These observations suggest that the aerosols observed in the center of the plume originated along with CO and NO_x from various power plants and vehicular traffic across the city, with the majority of the nanoparticles constituting the Aitken mode directly

emitted from the oil and natural gas-fired power plants and organically mediated new particle formation.

Despite considerable dilution, the observed number concentrations of CCN (N_{CCN}) at supersaturations (SS) 0.23 and 0.5% were a factor of ~ 3.5 higher than the corresponding background values and remained nearly steady or even increased with aging (Fig. 2A), indicating substantial growth of nanoparticles to CCN-active sizes in the plume. The total particulate sulfate and nitrate mass concentrations were relatively much smaller compared to organics (Fig. 2B). In contrast, despite appreciable dilution, the total particulate organic mass concentration increased from $1.2 \pm 0.2 \mu\text{g m}^{-3}$ in the first plume transect to $2 \pm 0.02 \mu\text{g m}^{-3}$ in the third transect, indicating substantial SOA formation. Although the fourth transect show continued growth of the nanoparticles, a slight decrease in the total organics mass concentration to $1.5 \pm 0.1 \mu\text{g m}^{-3}$ was likely caused by a shift in the overall balance of SOA formation and dilution rates. Positive matrix factorization (PMF) analysis of the high-resolution mass spectra of organics revealed that the fraction of oxygenated organic aerosol increased as the fraction of hydrocarbon-like organic aerosol decreased with plume age (44), consistent with SOA formation due

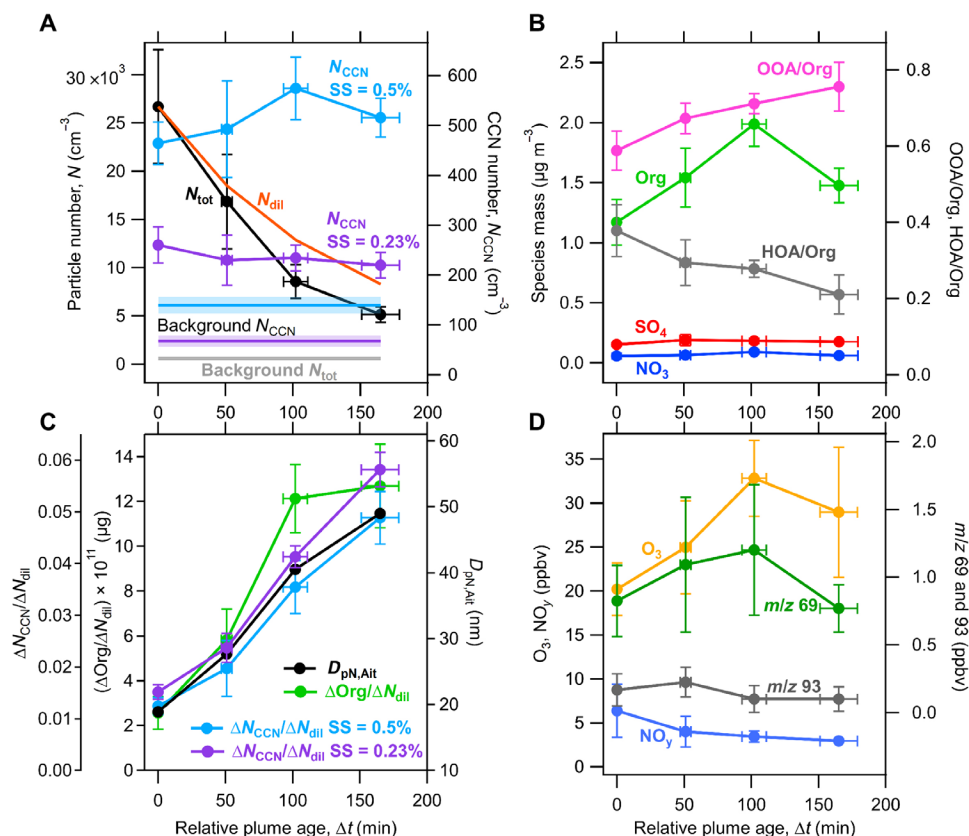


Fig. 2. Evolution of various properties (1-min average) along plume peaks due to photochemical aging and dilution. Plume age is estimated relative to the first downwind transect P1. **(A)** Observed total aerosol number concentration (N_{tot}) and that predicted due to dilution only (N_{dil}) along with CCN number concentrations at supersaturations (SSs) = 0.23 and 0.5%. **(B)** Mass concentrations of total particulate organics (Org), sulfate (SO_4), and nitrate (NO_3) along with oxygenated organic aerosol (OOA)/Org and hydrocarbon-like organic aerosol (HOA)/Org ratios. **(C)** Dilution-corrected Org mass and CCN number concentrations along with Aitken number mode diameter ($D_{\text{pN,Ait}}$). **(D)** Gas-phase mixing ratios of ozone (O_3), total odd nitrogen (NO_y), isoprene [mass-to-charge ratio (m/z) 69], and toluene (m/z 93). The vertical error bars (and shaded areas) represent one SD for 1-min averages, while the horizontal error bar represents error in the estimated relative plume age due to one SD in the average wind speed over all four transects.

to condensation of oxidation products of VOCs. To account for dilution, we normalize the background-corrected values of CCN number (ΔN_{CCN}) and Org mass (ΔOrg) concentrations by background-corrected particle number concentration predicted by dilution only (ΔN_{dil}). Figure 2C clearly shows that the rapid increase in the dilution-corrected Org mass concentration due to SOA formation in the urban plume causes the Aitken mode particles ($D_{\text{pN,Ait}}$) to rapidly grow and consequently increase the dilution-corrected CCN number concentrations at both SS values.

Photochemically produced ozone also displayed a markedly similar evolution in the plume as the organic aerosol, while the sum of all odd nitrogen species (NO_y) decreased due to dilution (Fig. 2D). Anthropogenic VOCs such as benzene and toluene were close to detection limits of approximately 0.05 ppbv in background air but increased in the plume. Biogenic monoterpenes were mostly close to or below their detection limits of approximately 0.2 ppbv, both in the plume and background air, while isoprene (Fig. 2D) and its first-generation oxidation products (mass-to-charge ratio 71) remained relatively steady in the plume at 1.0 ± 0.4 ppbv and 1.5 ± 0.3 ppbv, respectively (2.8 ± 0.7 ppbv and 1.1 ± 0.2 ppbv, respectively, in the background air). A lifetime of 2.7 hours was estimated for isoprene due to its reaction with hydroxyl radicals (OH), whose

concentration was observed at $1 \pm 0.2 \times 10^6$ molecule cm^{-3} at the T3 ground site between 10:36 and 11:36 LST. However, the lack of monotonic depletion of isoprene with plume age suggests the loss due to reaction with OH was roughly balanced by fresh emissions as the plume was advected westward over the forest. Although isoprene was the dominant observed VOC in this particular episode, about 20% of the total SOA formed in the plume could have also come from unmeasured VOCs of anthropogenic origin (24, 50) and, possibly to a much smaller extent, from sesquiterpenes (51).

Interpreting the mechanism of nanoparticle growth

Photooxidation of isoprene forms numerous products, some of which can lead to SOA formation via different gas-particle partitioning mechanisms. One of the widely studied mechanism involves reactive uptake of isoprene epoxidols (IEPOX) onto acidic aerosols to form SOA (52, 53). However, aerosol sulfate was completely neutralized by ammonium in the plume (fig. S4), and PMF analysis estimated that less than 5% of the total organic mass was composed of IEPOX SOA (44, 54), suggesting that this pathway likely played a minor role in the growth of the nanoparticles. Isoprene SOA can also form via gas-particle partitioning of isoprene dihydroxy dihydroperoxide and several other oxidized SVOCs with volatilities

ranging from about 2 to 30 $\mu\text{g m}^{-3}$, with some SVOCs gradually forming oligomers in the particle phase (22, 23, 33, 55). If the pre-existing organic aerosol is liquid-like, then these SVOCs would tend to partition into larger particles that dominate the organic mass (25). While organic aerosols in the background air around Manaus exist in a liquid-like state (56), those of urban origin or influence were found to be semisolid even at 75% RH (57), in which case aerosol growth kinetics would be controlled by in-particle bulk diffusion of the condensing SVOCs. In each case, the impacts of the condensing compound's volatility, its particle-phase bulk diffusivity, and particle-phase reactivity will be reflected in the resulting aerosol size distribution evolution (17, 33, 34, 39).

Here, we analyzed the observations of aerosol size distribution evolution in combination with simulations with the Model for Simulating Aerosol Interactions and Chemistry (MOSAIC) (18, 58) sectional aerosol box model in a Lagrangian framework (see the "Lagrangian aerosol box model" section) to probe the dominant mechanism responsible for SOA formation and the associated growth of the nanoparticles. The in-plume aerosol size distribution in the model was initialized with that observed at P1, and the background aerosol size distribution was set to that observed at B (shown in Fig. 1A). The size-distributed aerosol composition of in-plume and background aerosols were initialized on the basis of the bulk aerosol composition observed at P1 and B, respectively. New particle formation and primary aerosol emissions were not considered during the downwind plume transport. With monoterpenes mostly close to or below their detection limits, isoprene was deemed as the dominant SOA precursor and its mixing ratio was held constant at 1 ppbv. However, because isoprene is the sole VOC that formed SOA in the model, it also represents the pool of other unmeasured SOA precursors. A recent modeling study showed that NO_x emissions from Manaus were responsible for OH radical concentrations greater than 1×10^6 molecule cm^{-3} in the urban plume compared to an order of magnitude lower concentrations in the background air (50). The in-plume OH radical concentration was thus held constant at 1×10^6 molecule cm^{-3} in the present box model. Although it takes several steps to produce several condensable products from isoprene photooxidation, the isoprene + OH reaction in the model was parameterized to directly form only one condensable SVOC with an assumed molecular weight of 168 g mol^{-1} and prescribed gas-phase yield (α_g), volatility (C^*), bulk diffusivity (D_b), and particle-phase second-order reaction rate constant (k_c) that represents oligomer formation. The purpose of using this simple reaction scheme was to circumvent the complex gas-phase photochemistry of isoprene and other unmeasured VOCs and instead focus on the effects of the volatility, bulk diffusivity, and reactivity of the condensable organics on particle size-dependent growth dynamics. Dilution of in-plume aerosol with background aerosol was treated as a first-order process with the estimated dilution rate of $\lambda = 7.4 \times 10^{-3} \text{ min}^{-1}$. For a set of prescribed C^* and D_b in a given simulation, α_g was adjusted such that the predicted total aerosol mass concentrations after $\Delta t = 102$ and 165 min matched the values observed at P3 and P4, respectively. By constraining the mass of newly formed SOA in this manner, the model thus simulated the effects of C^* , D_b , and k_c on the evolution of aerosol size distribution for evaluation against that observed at P3 and P4. In this approach, the consequence of holding the OH and surrogate parent VOC concentrations constant is that the predicted temporal evolution of SOA along the trajectory could be slightly off although the final value matches the observed value.

Independently, without any additional tuning, the predicted total aerosol number concentrations above 10 nm were in excellent agreement (within ~5%) with those observed at P3 and P4. This result confirms that the total aerosol number concentration in the plume was mainly governed by dilution while coagulation played a minor role and lends support to initializing the model with the aerosol size distribution observed at P1 and assuming Lagrangian transport to downwind locations.

Figure 3 shows the comparison of the observed aerosol size distributions at P3 with those simulated using different values of C^* and D_b for the condensing SVOC in liquid-like and semisolid scenarios for $k_c = 0 \text{ m}^3 \text{ mol}^{-1} \text{ s}^{-1}$. Depending on the combination of the values for C^* and D_b , the required α_g ranged from 0.47 to 0.95 (table S1). These rather high values of α_g suggest that some SOA was formed from other VOCs besides isoprene, such as a pool of unmeasured anthropogenic VOCs in the plume. In the four liquid-like scenarios, $D_b > 10^{-10} \text{ cm}^2 \text{ s}^{-1}$ for particles in all size bins, and C^* for the oxidation product was set at 0.1, 1, 5, and 10 $\mu\text{g m}^{-3}$. None of the liquid-like scenarios was able to reproduce both the observed aerosol number and volume size distributions (Fig. 3). Although the liquid-like scenario with $C^* = 0.1 \mu\text{g m}^{-3}$ was able to grow the Aitken number mode to its observed size, it substantially overpredicted its peak height and the growth of the Acc1 volume mode diameter in the bimodal accumulation mode. The simulated number and volume size distributions with $C^* = 0 \mu\text{g m}^{-3}$ (not shown for clarity) were nearly identical to those with $C^* = 0.1 \mu\text{g m}^{-3}$, indicating that neither the condensation of extremely low volatility organic compounds nor a reactive uptake mechanism, which would have caused the size distribution to respond in the same manner as nonvolatile vapor condensation, was the dominant mechanism. The performance of the liquid-like scenario with $C^* = 1 \mu\text{g m}^{-3}$ was also similar to that with $C^* = 0.1 \mu\text{g m}^{-3}$. However, the liquid-like scenarios with $C^* = 5$ and 10 $\mu\text{g m}^{-3}$ progressively underpredicted the growth of the nanoparticle number mode and overpredicted the growth of the two accumulation volume modes, consistent with the expectation that SVOCs with increasing volatility favorably partition to the largest liquid-like particles that dominate the organic mass (25). Liquid-like scenarios with multiple oxidation products were also tested, but they too overpredicted the peak height of the Aitken number mode and the growth of the Acc1 volume mode diameter (fig. S5). All liquid-like scenarios also failed to reproduce the observed pronounced increase in the Acc1 volume mode peak height and the concurrent decrease of the Acc2 volume mode observed at P3. These sensitivity tests also show that the shapes of the predicted aerosol number and volume size distributions are more sensitive to the volatility of the condensable products than the number of condensable products.

However, the observed growth and shape of the Aitken number mode and the lack of growth of the Acc2 volume mode could be reproduced reasonably well by dynamically partitioning an SVOC with $C^* = 5 \mu\text{g m}^{-3}$ with the assumption that particles greater than 160 nm (i.e., Acc2 mode) were viscous semisolids with an effective $D_b = 2.5 \times 10^{-15} \text{ cm}^2 \text{ s}^{-1}$, while all the smaller ones were still liquid-like with $D_b > 10^{-10} \text{ cm}^2 \text{ s}^{-1}$ (Fig. 3, C and D). Although the background SOA over the Amazon rainforest (56) and the freshly formed isoprene SOA in the growing nanoparticle mode (30, 59) are expected to be liquid-like at 80% RH, Bateman *et al.* (57) found the presence of nonliquid particles (190 nm in mobility diameter) with a low oxygen to carbon ratio (O:C) of 0.42 in air parcels influenced by Manaus

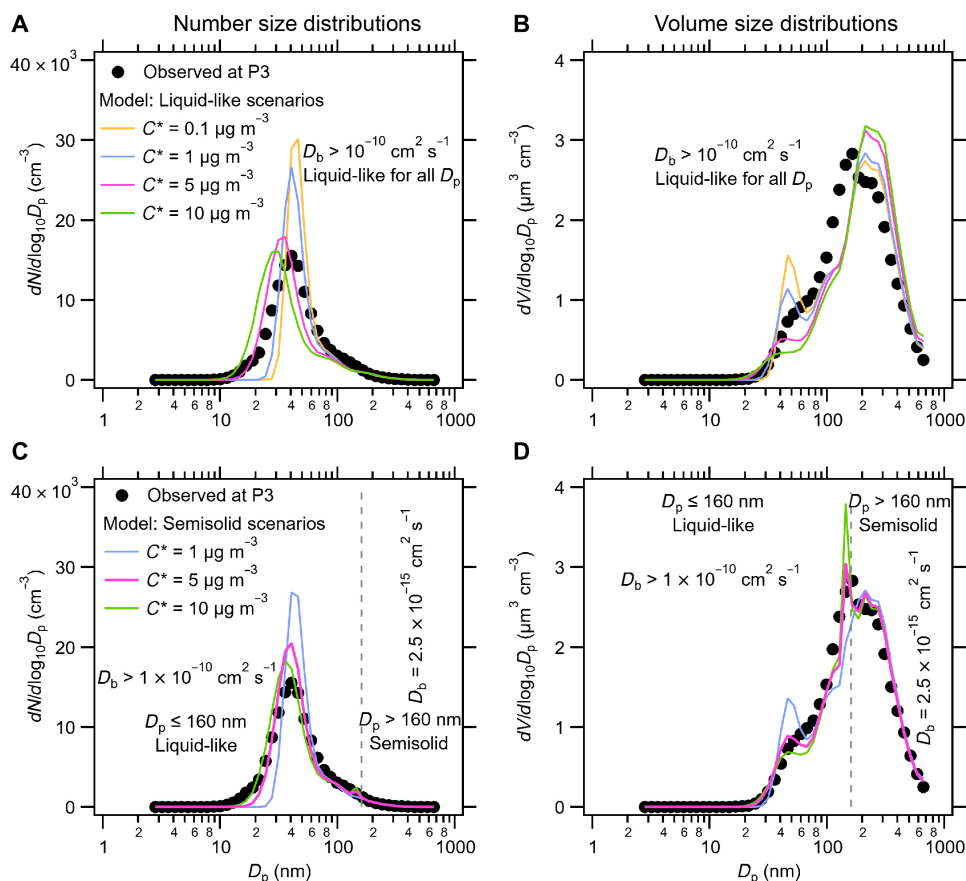


Fig. 3. Comparison of the observed aerosol size (D_p) distributions at P3 ($\Delta t = 102$ min) with those simulated with $k_c = 0 \text{ m}^3 \text{ mol}^{-1} \text{ s}^{-1}$ and different values of C^* and D_b . (A) Evaluation of modeled aerosol number size distributions for liquid-like scenarios. (B) Evaluation of aerosol volume size distributions for liquid-like scenarios. (C) Evaluation of modeled aerosol number size distributions for semisolid scenarios. (D) Evaluation of aerosol volume size distributions for semisolid scenarios.

emissions, suggesting that the Acc2 mode particles were viscous semi-solids that were likely composed of primary organic particles (i.e., directly emitted from fuel oil/diesel power plants and vehicular traffic) mixed with biogenic SOA (36). In this semisolid scenario, the hindered partitioning of the SVOC to the Acc2 volume mode particles effectively allowed more SVOC to be absorbed by the competing liquid-like Aitken mode, thereby rapidly growing it. Consequently, this scenario was also able to reproduce the pronounced increase in the Acc1 volume mode peak height as it gained some particles from the growing nanoparticle mode, while the Acc2 volume mode resisted growth due to bulk diffusion limitation. The semisolid scenario with $C^* = 10 \mu\text{g m}^{-3}$ was also able to reproduce the growth of the Aitken mode but overpredicted the increase of the Acc1 volume mode peak height. In comparison, the semisolid scenario with $C^* = 1 \mu\text{g m}^{-3}$ overpredicted the growth of the Aitken mode and could not reproduce the development of the Acc1 volume mode at all. Additional semisolid scenarios with $C^* \leq 0.1 \mu\text{g m}^{-3}$ produced results (not shown for clarity) similar to that obtained for liquid-like scenarios for the same C^* values. Similar conclusions were drawn from model evaluation using observations at P4 (fig. S6).

As mentioned earlier, SVOCs formed from isoprene photo-oxidation are known to form oligomers via particle-phase accretion reactions (22, 23, 33, 55). Figure 4 shows the comparison of the observed aerosol size distributions at P3 with those simulated by a

condensing SVOC of $C^* = 5 \mu\text{g m}^{-3}$ with three different values for its second-order reaction rate constant (k_c), including $k_c = 0$ for reference. The required α_g are given in table S2. In the case of $k_c = 2 \times 10^{-8} \text{ m}^3 \text{ mol}^{-1} \text{ s}^{-1}$, about 13% of the monomer SVOC was converted into dimers at P3, while an order of magnitude higher value of k_c resulted into 50% conversion. As before, none of the liquid-like scenarios was able to reproduce the observed size distributions (Fig. 4, A and B). In the semisolid scenario with $k_c = 2 \times 10^{-8} \text{ m}^3 \text{ mol}^{-1} \text{ s}^{-1}$, the predicted number and volume size distributions compared well with the observed distributions and were nearly identical to those predicted with $k_c = 0$ (Fig. 4, C and D). However, $k_c = 2 \times 10^{-7} \text{ m}^3 \text{ mol}^{-1} \text{ s}^{-1}$ caused the predicted size distributions to deviate further from those observed, suggesting that oligomerization likely occurred at a slower rate.

Overall, our analysis suggests that the dominant mechanism of SOA formation that rapidly grew the nanoparticles likely involved isoprene and possibly other unmeasured precursors forming multiple SVOCs with C^* ranging from about 2 to 10, with a nominal value of about $5 \mu\text{g m}^{-3}$ that mostly partitioned into liquid-like particles smaller than about 160 nm instead of the larger ones that were semisolid and likely experienced gradual oligomerization with aging. Condensation of ELVOCs and rapid reactive uptake mechanism are also possible, although it appears that they may have played a minor role in the growth of the nanoparticles after they grew to about

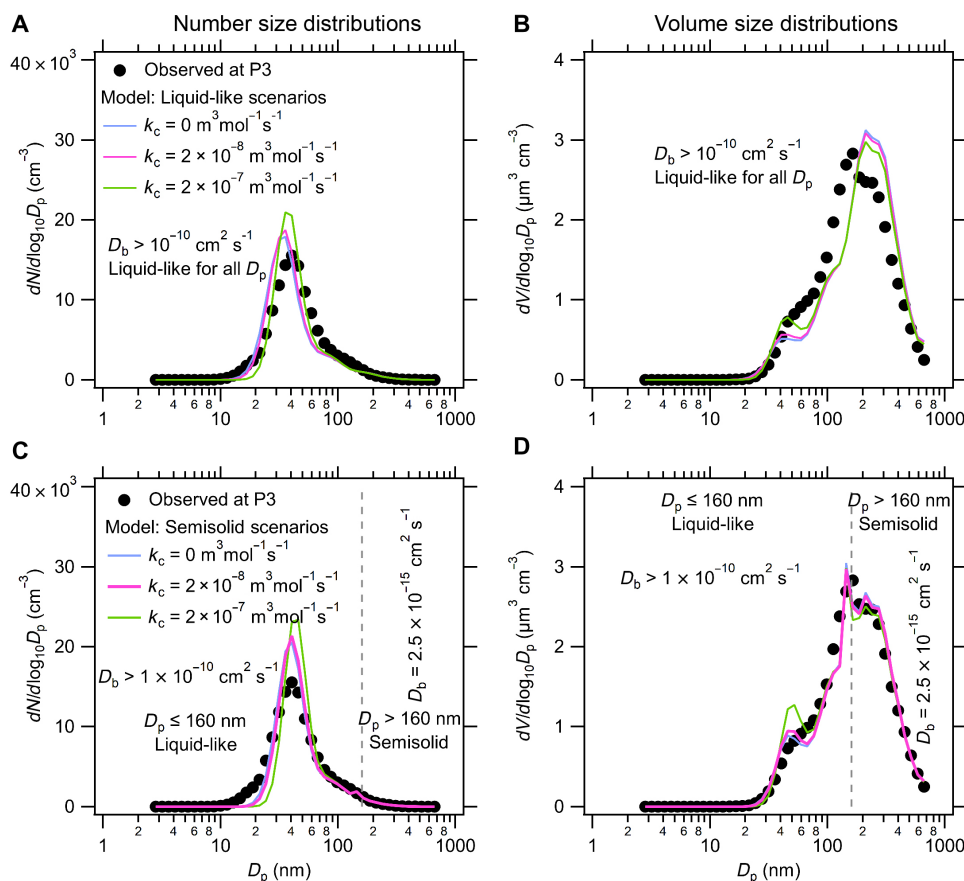


Fig. 4. Comparison of the observed aerosol size (D_p) distributions at P3 ($\Delta t = 102$ min) with those simulated with $C^* = 5 \mu\text{g m}^{-3}$ and different values of k_c and D_b . (A) Evaluation of modeled aerosol number size distributions for liquid-like scenarios. (B) Evaluation of aerosol volume size distributions for liquid-like scenarios. (C) Evaluation of modeled aerosol number size distributions for semisolid scenarios. (D) Evaluation of aerosol volume size distributions for semisolid scenarios.

20 nm diameter. One of the main consequences of the rapid nanoparticle growth was the increase in the number concentrations of SOA-dominated particles that can act as CCN. The size- and phase-dependent dynamic SOA partitioning mechanism used in this study should be generally applicable under a variety of conditions, and its impact on CCN production can be quantified based on the measured aerosol size distribution and size-resolved aerosol composition evolution.

Impacts of organic nanoparticle growth on clouds and precipitation

The Amazon rainforest during the wet season is characterized by pristine air, shallow warm clouds, and frequent rain showers. The transition of shallow to deep convective represents another important characteristic of Amazonian clouds (60). Perturbation in the naturally occurring CCN concentrations by Manaus emissions can alter both cloud and precipitation formation in the downwind region (61). An analysis of the aircraft observations collected during the wet season showed that pollution-affected clouds downwind of Manaus had 10 to 40% smaller effective diameters and up to 1000% higher cloud droplet concentrations (62). To examine the potential impacts of the rapid growth of anthropogenic nanoparticles on clouds and precipitation, we performed cloud-resolving model (see the “Cloud model” section) simulations using a grid spacing of 500 m with

spectral bin microphysics (SBM) for the clouds that occurred around and downwind of Manaus on the afternoon of 17 March 2014, as described in Fan *et al.* (49). Similar or even coarser resolutions have been used for shallow cloud simulations in other studies (63, 64).

During this episode, some shallow nonprecipitating cumulus transitioned to deeper, precipitating convection. The reason for simulating clouds on 17 March instead of 13 March is the lack of cloud formation downwind of Manaus during the morning aircraft flight on 13 March. The Manaus urban plume on 17 March was approximately in the same location as on 13 March (Fig. 5A), and the nanoparticles experienced similar rapid growth as well (Fig. 5B). However, the number concentrations of aerosols were affected by cloud and rain formation over parts of the plume as the plume was transported westward, thus making a careful analysis of the aerosol growth more complicated on 17 March than on 13 March. Figure 5 (C and D) illustrates the downwind plume locations (C1 to C3) and the associated droplet size distributions of shallow clouds sampled by the G-1 aircraft near their base at an altitude of about 1.25 km, MSL.

Two simulations were designed for 17 March with the same total aerosol number concentration of about 3800 cm^{-3} specified over Manaus up to 1 km altitude from 5:00 to 17:00 LST to mimic the continuous source of nanoparticles from Manaus (Fig. 6A) but with different aerosol size distributions (Fig. 6B). The shape of one corresponds to that observed at P1 (Fig. 1C) and represents no further

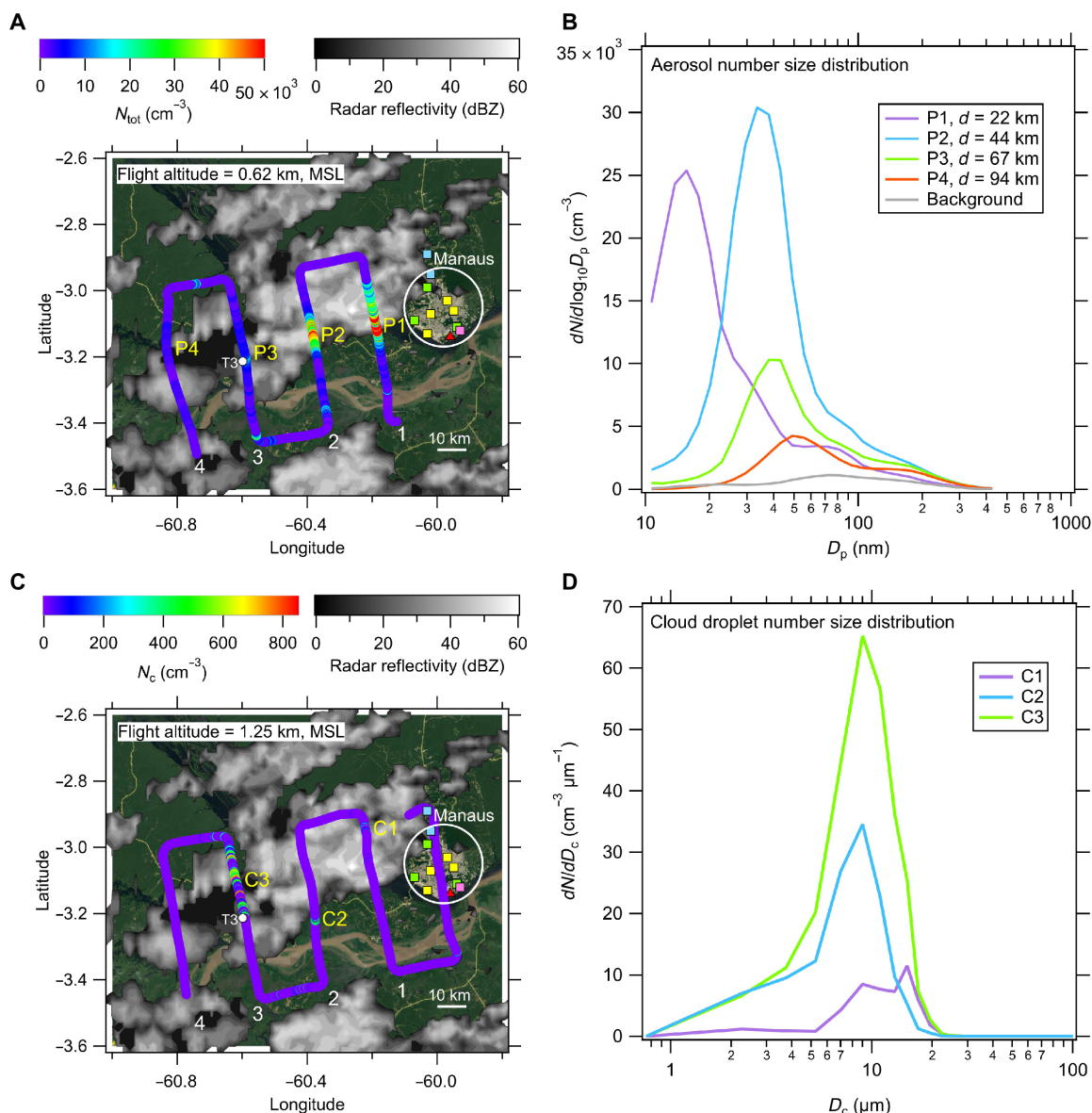


Fig. 5. Manaus urban plume on 17 March 2014. (A) Total aerosol number concentration (N_{tot}) along the G-1 aircraft flight path at 0.62 km, MSL altitude between 12:43 and 13:32 LST, with plume peaks denoted as P1 to P4. Colored squares and triangle are same as in Fig. 1A. Composite radar reflectivity (i.e., column maximum during the period from 12:47 to 13:35 LST) from the SIPAM S-band radar indicates portions of the urban plume that was affected by clouds and rain (see the “Precipitation characterization using SIPAM radar” section). (B) Observed aerosol number size distributions (1-min average) along the plume peaks and in background air. (C) Total cloud droplet number concentration (N_c) along the aircraft flight path at 1.25 km, MSL altitude between 13:45 and 14:35 LST, with shallow cloud samples in the plume denoted as C1 to C3. (D) Observed cloud droplet size distributions at C1 to C3.

growth of the Aitken number mode diameter beyond the initial growth to about 20 nm, referred to as the “limited growth” scenario, while the other corresponds to that observed at P4 (Fig. 1C) and represents sustained rapid growth to about 50 nm due to condensation of SVOCs, referred to as the “sustained growth” scenario. The initial aerosol size distribution and vertical profile for the background area (i.e., the area outside Manaus) used for both scenarios are also shown in Fig. 6 (A and B). As shown in Fig. 6 (C and D), these model configurations approximately represent the observed total aerosol number concentrations in the plume about 115 km downwind of Manaus, at which point the observed Aitken number mode diameter

had grown to 50 nm (location P4 in Fig. 5, A and B) and where shallow clouds started to form at 10:00 LST in the model. Thus, the differences in the predicted clouds and precipitation between the two simulations represent the effects of the shift in aerosol size distribution (without a change in number concentration) due to rapid growth of nanoparticles. The present study differs from the study of Fan *et al.* (49) that examined cloud-aerosol interactions in deep convective clouds associated with large quantities of ultrafine particles smaller than 50 nm added to the pristine background environment. The prescribed aerosol size distributions in our simulations are designed to isolate the effects of rapid nanoparticle growth on shallow

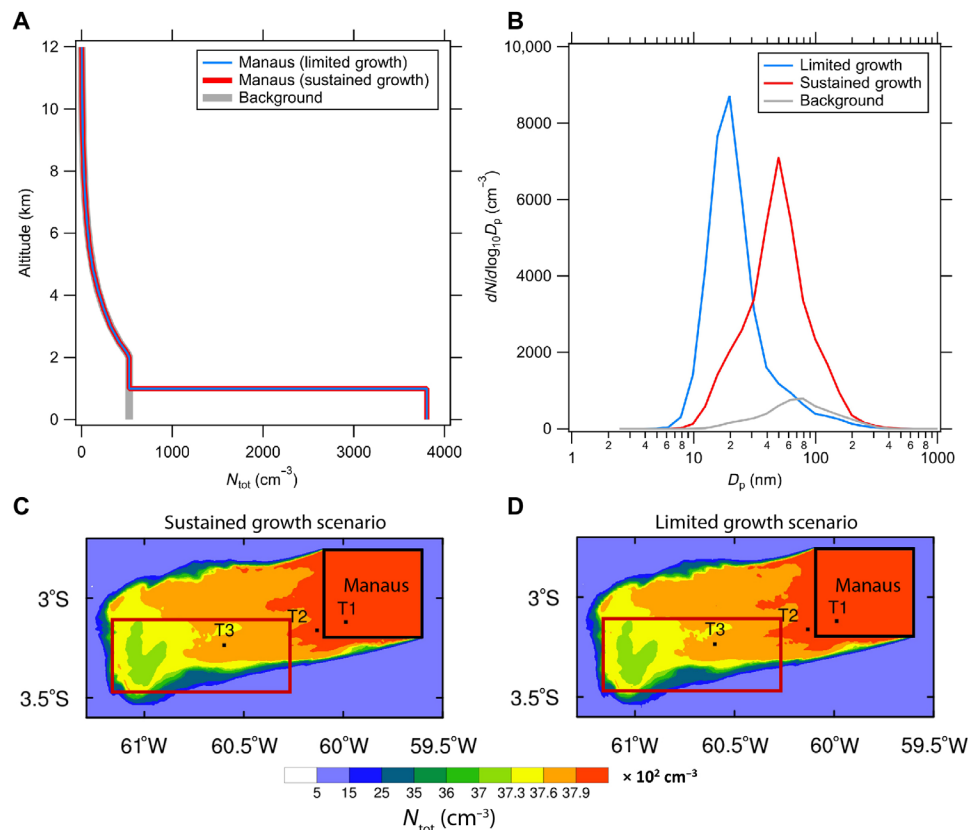


Fig. 6. Design of the limited and sustained nanoparticle growth scenarios for cloud-resolving model simulations. (A) Vertical distribution of aerosol concentrations specified over Manaus and held constant between 5:00 and 17:00 LST for the two scenarios along with the initial vertical distribution in the background air. (B) Aerosol number size distributions specified over Manaus for both scenarios and in the background air. Simulated aerosol number concentrations on 17 March 2014 at 08:00 LST for the (C) Sustained growth scenario and (D) limited growth scenario. The black box represents the area of Manaus, and the red box is the downwind area for which the simulated cloud and rain statistics are reported in Fig. 7.

clouds. Although the 500-m horizontal grid spacing seems coarse for simulating shallow cumulus clouds, our simulations with the subgrid-scale parameterization (i.e., Yonsei University planetary BL scheme), the Unified Noah land surface scheme, and SBM successfully predicted the shallow cumulus cloud water path in the sustained growth scenario similar to observations in a bulk sense (fig. S7). The observed cloud droplet size distribution at the base of shallow clouds (at downwind location C3 shown in Fig. 5C) is in excellent agreement with that simulated in the sustained growth scenario, distinctly different from that in the limited growth scenario (Fig. 7A). The simulated rainwater path and cloud fractions for both scenarios are shown in fig. S8.

Compared to the limited growth scenario, the sustained growth scenario resulted in a two- to threefold increase in the droplet nucleation rate and cloud droplet number mixing ratios around cloud bases during the shallow cloud stage period 10:00 to 11:00 LST (Fig. 7, B and C). The cloud water mass mixing ratio increased as well in the sustained growth scenario (Fig. 7D) (62). In the high humidity conditions over the Amazon Basin during the wet season, there is ample moisture for droplet condensational growth. As a result, there was only 10 to 22% reduction in the mean droplet effective radius in the sustained growth scenario compared to the limited growth scenario (Fig. 8A), thus resulting in relatively modest enhancements in the cloud albedo in the sustained growth scenario

(fig. S9). However, the reduction in the mean droplet effective radius slowed down the autoconversion process rate (i.e., the collision of cloud droplets to form raindrops) by one to two orders of magnitude, which caused a marked reduction in the raindrop number concentration (Fig. 8B) and rain mass mixing ratio (Fig. 8C). Consequently, surface rain at the shallow cloud stage greatly decreased in the sustained growth scenario, with a ~43% reduction in 1-hour accumulated rain for the shallow cloud period and ~32% reduction in the maximum rain rate. The rain rate probability distribution function between the two simulations changed (Fig. 8D), with more frequent drizzle rain (0.05 to 0.25 mm hour⁻¹) but a lack of relatively heavier rain (> 0.4 mm hour⁻¹) in the sustained growth scenario.

The cloud fractions around cloud bases were similar in the two scenarios because of the humid environment (fig. S8). However, the cloud fraction aloft increased greatly—more shallow clouds grew taller to altitudes above 2.5 km in the sustained growth scenario as compared to the limited growth scenario, with a ~60% increase in the cloud fraction above 2.5 km during the shallow cloud period 10:00 to 11:00 LST (Fig. 9A and fig. S8). This resulted in an enhancement of shallow-to-deep convective cloud transition in the sustained growth scenario as deep convective cloud fraction increased by up to 90% during the transition period 11:00 to 11:30 LST (Fig. 9B), with substantial reductions in shallow cloud fraction below 3 km (Fig. 9C). Thus, with the rapid, sustained growth of nanoparticles

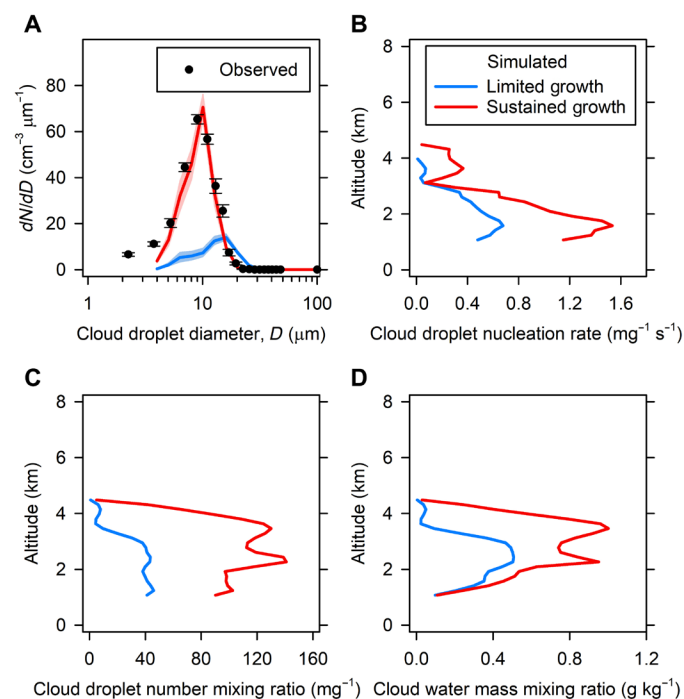


Fig. 7. Impacts of nanoparticle growth on shallow clouds. (A) Observed (filled black circles) and simulated mean cloud droplet number size distributions at the base of shallow clouds at the C3 location at ~ 1.2 -km MSL altitude (as shown in Fig. 5, A and B) for the limited growth (blue) and sustained growth (red) scenarios. The error bars and color shaded areas represent standard errors for the observed and simulated mean size distributions, respectively. The observed size distribution is calculated using shallow cloud samples with total droplet number concentration (N_t) between 400 and 700 cm^{-3} during 13:45 to 13:50 LST. The mean simulated cloud droplet number size distributions for both scenarios are calculated based on shallow clouds (hydrometeor mixing ratio $> 10^{-5}$ kg kg^{-1} and cloud top temperature $< 0^\circ\text{C}$) with N_t ranging from 90th to 99th percentile (approximately corresponding to 400 to 700 cm^{-3} in the sustained growth scenario) in the plume region indicated by the red box in Fig. 6C during 13:30 to 14:00 LST. Simulated mean vertical profiles of (B) cloud droplet nucleation rates, (C) cloud droplet number mixing ratios, and (D) cloud water mass mixing ratios during the shallow cloud stage period 10:00 to 11:00 LST over the shallow cloudy points with hydrometeor mixing ratio $> 10^{-5}$ kg kg^{-1} and cloud top temperature $< 0^\circ\text{C}$ in the red box in Fig. 6C.

over the humid Amazon, rain formation from shallow warm clouds is much less efficient, which allows an enhanced vertical growth of shallow clouds to form deeper clouds during the shallow cloud period. This results in an enhancement in shallow to deep convective cloud transition, with markedly more deep clouds and less shallow clouds during the transition period. The impact of the rapid nanoparticle growth on cloud and precipitation at the deep convective cloud stage was small, because almost all aerosols (small and large) were activated in both scenarios due to large updrafts.

Summary and outlook

As summarized by the schematic in Fig. 10, this study provided new insights into the growth mechanism responsible for the rapid growth of anthropogenic nanoparticles via SOA formation to CCN sizes and the subsequent impacts on clouds and precipitation, with implications beyond the exemplary case study of an isolated urban area amidst the Amazon rainforest. While ELVOCs are crucial for the

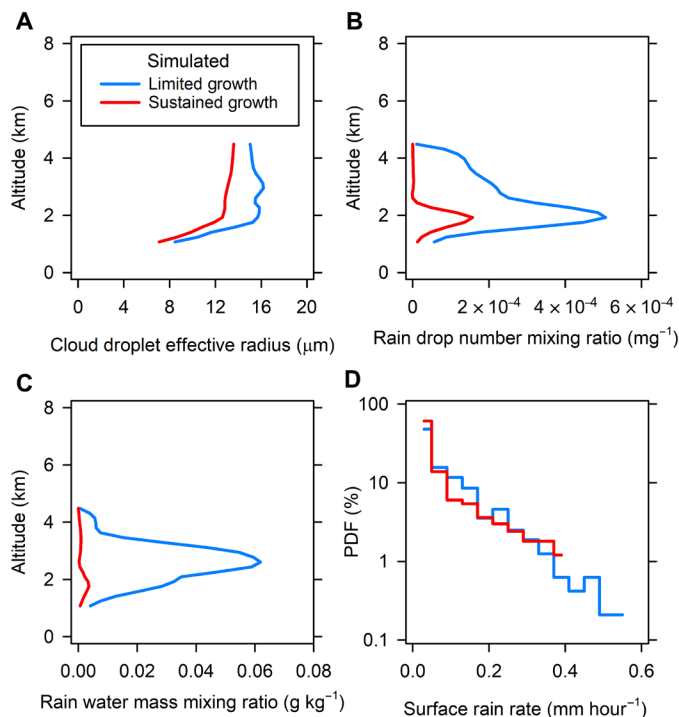


Fig. 8. Impacts of nanoparticle growth on rain during the shallow cloud period 10:00 to 11:00 LST. Simulated mean vertical profiles of (A) cloud droplet effective radius, (B) rain drop number mixing ratios, and (C) rainwater mass mixing ratios for the limited growth (blue) and sustained growth (red) scenarios. (D) Probability distribution functions (PDFs) of simulated surface rain rates, calculated by excluding values smaller than 0.01 mm hour^{-1} . All the calculations are for the plume region downwind indicated by the red box in Fig. 6C. Values in (A) to (C) are averaged over the shallow cloudy points that are identified with hydrometeor mixing ratio $> 10^{-5}$ kg kg^{-1} and cloud top temperature $< 0^\circ\text{C}$.

initial growth of nanoparticles smaller than 10 nm, our model analysis showed that sustained rapid growth of these particles from about 20 to 50 nm was largely due to condensation of SVOCs that were likely formed from isoprene and a pool of unmeasured anthropogenic VOCs. Moreover, it was necessary to dynamically partition the SVOCs to particles of different sizes and account for in-particle bulk diffusion limitations in semisolid particles to reproduce the observed growth of nanoparticles along with the evolution of aerosol number and volume size distributions. Although the equilibrium partitioning approach traditionally used in most SOA models may be able to reproduce the total mass, it may not accurately capture the growth of nanoparticles and the evolution of the overall aerosol size distribution. These findings have important implications for representing SOA formation and size- and phase-dependent particle growth mechanisms for CCN production in aerosol-climate models (65, 66).

In addition, using a real-case simulation at a cloud-resolving scale, this study provided an exemplary effect that the rapid growth of anthropogenic nanoparticles can exert on the shallow clouds and precipitation as well as on the transition of shallow to deep convection downwind of the Manaus urban area. While this case study is not a general proof, our results can be qualitatively applied to solar radiation driven shallow-to-deep transition cases occurring under

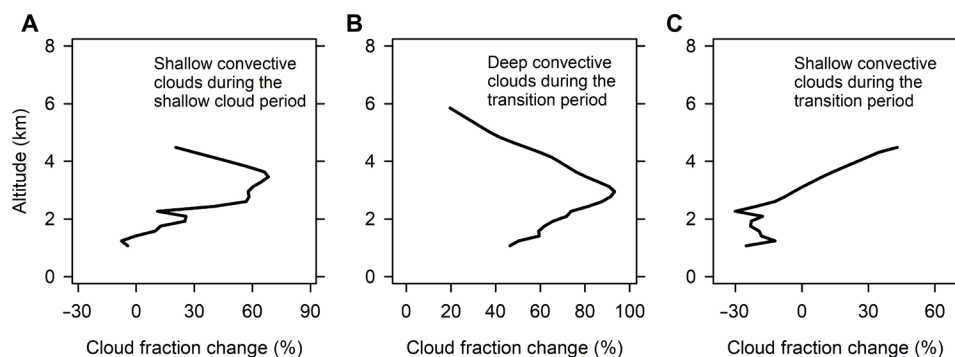


Fig. 9. Impacts of nanoparticle growth on cloud fractions. Vertical profiles of percentage change in the simulated cloud fraction in the sustained growth scenario relative to the limited growth scenario (A) for the shallow convective clouds during the shallow cloud period 10:00 to 11:00 LST and for the (B) deep convective clouds and (C) shallow convective clouds during the transition period 11:00 to 11:30 LST. Cloud fraction is calculated as a ratio of the cloudy points (hydrometeor mixing ratio $> 10^{-3} \text{ kg kg}^{-1}$) to the total grid points in the downwind plume region indicated by the red box in Fig. 6C.

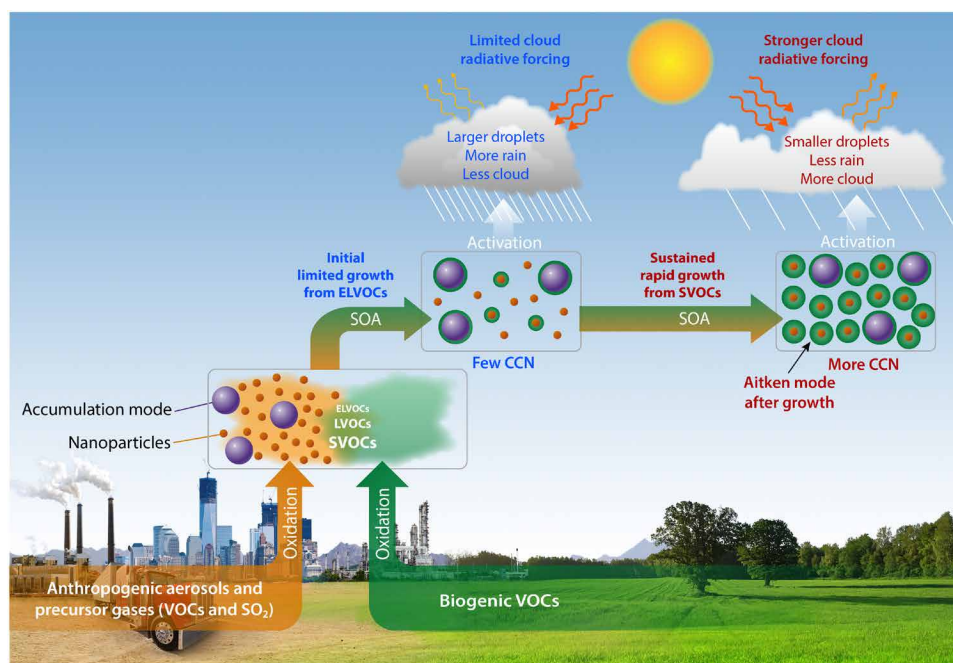


Fig. 10. Climate relevance of the rapid growth of anthropogenic nanoparticles via altered cloud radiative properties and precipitation. In addition to primary aerosols and VOCs, both anthropogenic and biogenic emissions also include NO_x , NH_3 , and amines, which can participate in new particle and secondary aerosol formations. Nanoparticles resulting from anthropogenic activities dominate the total aerosol number concentration in an urban pollution plume but are too small to serve as CCN. Their initial growth occurs from condensation of ELVOCs formed from oxidation of biogenic VOCs, resulting in the production of few new CCN. The more abundantly formed SVOCs are found to be responsible for the sustained rapid growth of the anthropogenic nanoparticles to CCN-relevant sizes. Higher CCN concentrations lead to the activation of smaller but more cloud droplets that suppress precipitation, reflect more incoming solar radiation, and cause stronger cloud radiative forcing.

similar meteorological conditions. Because condensable SVOCs form in abundance from the oxidation of anthropogenic and biogenic SOA precursors (22–24), the mechanistic insights developed in this study suggest that pollution nanoparticles are more likely than previously thought to grow to CCN sizes downwind of large urban centers in other forested regions and exert substantial impacts on clouds, precipitation, and climate. Further studies with fully coupled chemistry-aerosol-cloud models are needed in the future to investigate the coupling between anthropogenic nanoparticles, biogenic SOA, clouds, and precipitation and to improve the assessment of their impacts on weather and climate change.

MATERIALS AND METHODS

G-1 aircraft measurements

The Atmospheric Radiation Measurement Aerial Facility deployed several in situ instruments on the G-1 to measure trace gas concentrations, aerosol particle properties, cloud characteristics, atmospheric state and meteorological variables, and avionics parameters (41, 67). A fully automated isokinetic inlet was used to introduce ambient air into the G-1 for sampling aerosols. On the basis of the manufacturer wind tunnel test and peer-reviewed publications, this inlet operates for aerosol up to $5 \mu\text{m}$, with transmission efficiency around 50% at $1.5 \mu\text{m}$ (68). The air was dried to $<40\%$ RH by passage through

a Nafion dryer upstream of all aerosol instruments inside the G-1 cabin.

Condensation particle counters CPC-3025 and CPC-3010 were used to measure particle number concentrations for diameter greater than 3 and 10 nm, respectively (69), at a 1-s time resolution. Both CPCs were designed using the same principle, which is to detect particles by condensing butanol vapor on the particles to grow them to a large enough size that they can be counted optically. Both CPCs were calibrated in the laboratory before and after the field campaign, about 2 months apart.

A fast integrated mobility spectrometer (FIMS) inside the G-1 cabin measures the aerosol mobility size distribution from 10 to 400 nm in diameter at a time resolution of 1 s (70, 71). The ambient aerosol particles were charged after entering the FIMS inlet and then separated into different trajectories in an electric field based on their electrical mobility. The spatially separated particles grow into supermicrometer droplets in a condenser where SS of the working fluid is generated by cooling. At the exit of the condenser, a high-speed charge-coupled device camera captures the image of an illuminated grown droplet at high resolution. The aerosol number and volume size distributions shown in Fig. 1 (C and D) were extrapolated below 10 nm and above 400 nm by, respectively, fitting lognormal distributions to the observed Aitken mode number size distribution above 10 nm and the accumulation mode number size distribution below 400 nm.

The CCN number concentrations were measured at a time resolution of 1 s by a dual column CCN counter (CCN200, DMT) at two operating SSs (0.23 and 0.5%). The CCN counter is a continuous-flow thermal-gradient diffusion chamber that measures the total number concentration of aerosols that can act as CCN at each SS setting (72).

An Aerodyne high-resolution time-of-flight aerosol mass spectrometer was deployed on the G-1 to measure the chemical composition of nonrefractory aerosol particles between 60- and 1000-nm aerodynamic diameter (73). The AMS was operated only in the intermediate resolution “V” mass spectrometer mode with a time resolution of 13 s. The aerosol flow was periodically diverted through a high efficiency particulate air (HEPA) filter to remove particles, and these periods (at takeoff, landing, and sometime during the flight) were used to correct the spectra for background interferences. Data were processed using the high-resolution analysis techniques described in the literature (74). The high-resolution organic mass spectral data were analyzed by PMF to identify organic source factors using techniques described in the literature. Additional details on the operation of the AMS and the data analysis techniques, including PMF, are described by Shilling *et al.* (44).

An Ionicon quadrupole high-sensitivity proton-transfer reaction mass spectrometry (PTR-MS) was used to measure the concentration of VOCs (75). The PTR-MS was operated in an ion-monitoring mode in which a predetermined list of masses was sequentially measured with a complete cycle through the mass scan list taking 3.5 s. The PTR-MS sampled air through a separate, forward-facing inlet. Air was periodically diverted through a heated Shimadzu catalyst, which catalytically removed VOCs without disturbing ambient RH. These background measurements were used to correct the measured VOC signals. Multipoint calibrations were regularly performed in the field using a cylinder of known VOC concentrations. Additional details on the PTR-MS operation are described by Shilling *et al.* (44).

A fast cloud droplet probe (FCDP; SPEC Inc.) measured cloud droplet size distribution ranging from 1 to 50 μm . The FCDP is a compact, lightweight forward-scattering cloud particle spectrometer that measures cloud droplet size and concentration with up to 100-Hz sampling rate using a laser that scatters off the droplets into collection lens optics and is split and redirected toward two detectors. The FCDP bins the droplets into 20 bins ranging between 1 and 50 μm , with an accuracy of approximately 3 μm in diameter (62, 76). Bin sizes were calibrated using glass beads at several sizes in the total range. In this study, we used 1-Hz FCDP data. Shattering effects were filtered from the measured droplet size distributions with the built-in feature of the provided software.

BL height estimation using Doppler lidar

Estimates of the planetary BL depth were obtained from a ground-based scanning coherent Doppler lidar that was deployed approximately 65 km west-south-west of Manaus at the T3 ground site (3° 12' 47.6" S, 60° 35' 53.8" W). This instrument was operated with a fixed scan schedule consisting of vertical stares and plan-position-indicator (PPI) scans. The PPI scans were performed once every 15 min and took about 40 s to execute. Most of the time was spent staring vertically, making measurements of clear-air vertical velocity profiles in the lower troposphere with a temporal resolution of about 1 s and a height resolution of 30 m. The 1-s vertical velocity measurements were processed to yield height-resolved estimates of vertical velocity variance using a 30-min averaging time interval. The variances were computed using the noise correction method described by Lenschow *et al.* (77). Estimates of the mixed layer depth were obtained by applying a threshold of 0.01 $\text{m}^2 \text{s}^{-2}$ to the variance profiles. The mixed layer depth was determined from the maximum height where the vertical velocity variance exceeded the threshold (78).

Plume dilution rate estimation

Urban plume dilution was treated as a first-order process, and the dilution constant, λ (min^{-1}), was estimated from the rate at which the plume cross-section area (A) increased with time (t)

$$\lambda = \frac{1}{A} \frac{dA}{dt} = \frac{d \ln A}{dt} = \frac{\Delta \ln A}{\Delta t} = \frac{\Delta \ln(W \times H)}{\Delta t} = \frac{\ln[(W_f \times H_f)/(W_i \times H_i)]}{\Delta t} \quad (1)$$

where W is the plume width and H is the height of the BL in which the plume is assumed to be well mixed; subscripts i and f refer to initial and final values, respectively. As estimated from the spatial distribution of the observed total aerosol number concentration in the first and fourth G-1 transects, the width of the plume appears to have doubled (Fig. 1A). During the time ($\Delta t = 165$ min), the plume was advected from the location of the first transect to the fourth, and the mixed layer height grew from 648 to 1098 m (fig. S3). The horizontal dispersion and vertical mixing in the growing BL together yield an overall dilution constant of $\lambda = 7.4 \times 10^{-3} \text{ min}^{-1}$.

Lagrangian aerosol box model

Aerosol growth simulations were performed with the sectional aerosol box model MOSAIC (18, 58). MOSAIC treats coagulation between different particle size bins and dynamically partitions gases simultaneously to all size bins by considering compound volatility (C^*), gas-phase diffusion (D_g), interfacial mass accommodation (α_m),

in-particle bulk diffusion (D_b), and reversible particle-phase reactions. In this study, the values of D_g and α_m were assumed constant at $0.05 \text{ cm}^2 \text{ s}^{-1}$ and 0.1 (34), respectively, while C^* and D_b were prescribed different values with the goal of identifying the dominant aerosol growth mechanism. Particle-phase diffusion is treated using a combination of (i) an analytical quasi-steady-state treatment for the diffusion-reaction process within the particle phase for fast-reacting organic compounds such that the time scales for their particle-phase concentrations to reach quasi-steady state are shorter than 1 min and (ii) a two-film theory approach for slow- and non-reacting organic compounds (18). For this study, ammonium sulfate was assumed to be fully deliquesced at $\text{RH} = 80\%$. Hygroscopicity of organics was assumed to be 0.1 (79). Preexisting particulate organic species were assumed to have a molecular weight of 200 g mol^{-1} . The thermodynamic driving force for mass transfer is based on Raoult's law such that preexisting organics and liquid water act as solvents in absorbing the condensing organic vapors. The logarithmically spaced bin structure used in MOSAIC was the same as that of the particle size distribution data provided by FIMS. The transfer of particles between bins due to growth or shrinkage was calculated using a two-moment approach. Coagulation was turned on in the simulations.

Cloud model

The model simulations were performed using the Weather Research and Forecasting model v3.6.1 with the SBM for a locally occurring system occurring on 17 March 2014, following Fan *et al.* (49). The detailed domain configurations, forcing data, dynamics, and physics settings also follow Fan *et al.* (49). Briefly, two nested domains with horizontal grids of 1 and 0.5 km were used with 51 vertical levels up to 50 hPa. The numbers of horizontal grid points for domain 1 and domain 2 were 1000×1000 and 450×450 , respectively. Domain 2 was run with the "nesting down" approach, with the initial and boundary data produced by domain 1 simulations. Two sensitivity simulations were conducted over domain 2 for this study. The only difference between the two simulations was the aerosol size distribution specified over Manaus (the black box in Fig. 6C) with the same total aerosol number concentration, representing the sustained rapid growth of Aitken number mode diameter to 50 nm (referred to as sustained growth scenario) and no growth beyond 20 nm (referred to as limited growth scenario) as shown in Fig. 6C. The total aerosol number concentration over Manaus was set at 3800 cm^{-3} up to 1 km over Manaus for both simulations as shown in Fig. 6A. The vertical distribution and aerosol size distribution for the background area are also shown in Fig. 6 (A and B). The total aerosol concentration for the background was about 500 cm^{-3} near the surface and is assumed to be uniform below 2-km altitude and decrease exponentially above 2-km altitude. An overall hygroscopicity of 0.12 was prescribed for all aerosols based on their observed bulk composition of organics and inorganics (49). Note that the Manaus aerosol source was only turned on during the daytime from 5:00 to 17:00 LST to mimic reality. The simulated spatial extent of the aerosol plumes in the sustained growth and limited growth scenarios at 8:00 LST on 17 March (after 1-day simulation) are similar but with different size distributions (Fig. 6, C and D).

Precipitation characterization using SIPAM radar

The SIPAM (Sistema de Proteção da Amazônia) radar is an S-band Doppler weather radar, single polarization, with a 2° beam width

and radial resolution of 0.5 km. The radar was located at the Manaus military airport and made volume scans every 12 min at 17 elevations. The observations were quality-controlled and interpolated to a fixed three-dimensional grid at horizontal and vertical resolutions of 2 and 0.5 km, respectively (80). The horizontal grid size is 482 km^2 , and the vertical grid extends from 0.5 to 20 km.

SUPPLEMENTARY MATERIALS

Supplementary material for this article is available at <https://science.org/doi/10.1126/sciadv.abj0329>

REFERENCES AND NOTES

- O. Boucher, *et al.*, in *Climate Change 2013: The Physical Science Basis. Contribution of Working Group I to the Fifth Assessment Report of the Intergovernmental Panel on Climate Change*, T. F. Stocker *et al.*, Eds. (Cambridge Univ. Press, Cambridge, United Kingdom and New York, NY, USA, 2013), chap. 7, pp. 571–658.
- R. J. Charlson, S. E. Schwartz, J. M. Hales, R. D. Cess, J. A. Coakley Jr., J. E. Hansen, D. J. Hofmann, Climate forcing by anthropogenic aerosols. *Science* **255**, 423–430 (1992).
- J. H. Seinfeld, C. Bretherton, K. S. Carslaw, H. Coe, P. J. DeMott, E. J. Dunlea, G. Feingold, S. Ghan, A. B. Guenther, R. Kahn, I. Kraucunas, S. M. Kreidenweis, M. J. Molina, A. Nenes, J. E. Penner, K. A. Prather, V. Ramanathan, V. Ramaswamy, P. J. Rasch, A. R. Ravishankara, D. Rosenfeld, G. Stephens, R. Wood, Improving our fundamental understanding of the role of aerosol-cloud interactions in the climate system. *Proc. Natl. Acad. Sci. U.S.A.* **113**, 5781–5790 (2016).
- D. Rosenfeld, Y. Zhu, M. Wang, Y. Zheng, T. Goren, S. Yu, Aerosol-driven droplet concentrations dominate coverage and water of oceanic low-level clouds. *Science* **363**, eaav0566 (2019).
- S. Twomey, The influence of pollution on the shortwave albedo of clouds. *J. Atmos. Sci.* **34**, 1149–1152 (1977).
- B. A. Albrecht, Aerosols, cloud microphysics, and fractional cloudiness. *Science* **245**, 1227–1230 (1989).
- D. Rosenfeld, U. Lohmann, G. B. Raga, C. D. O'Dowd, M. Kulmala, S. Fuzzi, A. Reissell, M. O. Andreae, Flood or Drought: How Do Aerosols Affect Precipitation? *Science* **321**, 1309–1313 (2008).
- T. C. Bond, B. Wehner, A. Plewka, A. Wiedensohler, J. Heintzenberg, R. J. Charlson, Climate-relevant properties of primary particulate emissions from oil and natural gas combustion. *Atmos. Environ.* **40**, 3574–3587 (2006).
- E. Brewer, Y. Li, B. Finken, G. Quartucy, L. Muzio, A. Baez, M. Garibay, H. S. Jung, $\text{PM}_{2.5}$ and ultrafine particulate matter emissions from natural gas-fired turbine for power generation. *Atmos. Environ.* **131**, 141–149 (2016).
- T. Ronkko, H. Kuuluvainen, P. Karjalainen, J. Keskinen, R. Hillamo, J. V. Niemi, L. Pirjola, H. J. Timonen, S. Saarikoski, E. Saukko, A. Järvinen, H. Silvennoinen, A. Rostedt, M. Olin, J. Yli-Ojanperä, P. Nousiainen, A. Kousa, M. D. Maso, Traffic is a major source of atmospheric nanocluster aerosol. *Proc. Natl. Acad. Sci. U.S.A.* **114**, 7549–7554 (2017).
- D. V. Spracklen, K. S. Carslaw, M. Kulmala, V. M. Kerminen, G. W. Mann, S. L. Sihto, The contribution of boundary layer nucleation events to total particle concentrations on regional and global scales. *Atmos. Chem. Phys.* **6**, 5631–5648 (2006).
- I. Riipinen, T. Yli-Juuti, J. R. Pierce, T. Petäjä, D. R. Worsnop, M. Kulmala, N. M. Donahue, The contribution of organics to atmospheric nanoparticle growth. *Nat. Geosci.* **5**, 453–458 (2012).
- Q. Zhang, J. L. Jimenez, M. R. Canagaratna, J. D. Allan, H. Coe, I. Ulbrich, M. R. Alfarra, A. Takami, A. M. Middlebrook, Y. L. Sun, K. Dzepina, E. Dunlea, K. Docherty, P. F. DeCarlo, D. Salcedo, T. Onasch, J. T. Jayne, T. Miyoshi, A. Shimono, S. Hatakeyama, N. Takegawa, Y. Kondo, J. Schneider, F. Drewnick, S. Borrmann, S. Weimer, K. Demerjian, P. Williams, K. Bower, R. Bahreini, L. Cottrell, R. J. Griffin, J. Rautiainen, J. Y. Sun, Y. M. Zhang, D. R. Worsnop, Ubiquity and dominance of oxygenated species in organic aerosols in anthropogenically-influenced Northern Hemisphere midlatitudes. *Geophys. Res. Lett.* **34**, L13801 (2007).
- J. L. Jimenez, M. R. Canagaratna, N. M. Donahue, A. S. H. Prevot, Q. Zhang, J. H. Kroll, P. F. DeCarlo, J. D. Allan, H. Coe, N. L. Ng, A. C. Aiken, K. S. Docherty, I. M. Ulbrich, A. P. Grieshop, A. L. Robinson, J. Duplissy, J. D. Smith, K. R. Wilson, V. A. Lanz, C. Hueglin, Y. L. Sun, J. Tian, A. Laaksonen, T. Raatikainen, J. Rautiainen, P. Vaattovaara, M. Ehn, M. Kulmala, J. M. Tomlinson, D. R. Collins, M. J. Cubison, E. J. Dunlea, J. A. Huffman, T. B. Onasch, M. R. Alfarra, P. I. Williams, K. Bower, Y. Kondo, J. Schneider, F. Drewnick, S. Borrmann, S. Weimer, K. Demerjian, D. Salcedo, L. Cottrell, R. Griffin, A. Takami, T. Miyoshi, S. Hatakeyama, A. Shimono, J. Y. Sun, Y. M. Zhang, K. Dzepina, J. R. Kimmel, D. Sueper, J. T. Jayne, S. C. Herndon, A. M. Trimborn, L. R. Williams, E. C. Wood, A. M. Middlebrook, C. E. Kolb, U. Baltensperger, D. R. Worsnop, Evolution of organic aerosols in the atmosphere. *Science* **326**, 1525–1529 (2009).

15. I. Riipinen, J. R. Pierce, T. Yli-Juuti, T. Nieminen, S. Häkkinen, M. Ehn, H. Junninen, K. Lehtipalo, T. Petäjä, J. Slowik, R. Chang, N. C. Shantz, J. Abbatt, W. R. Leaitch, V. M. Kerminen, D. R. Worsnop, S. N. Pandis, N. M. Donahue, M. Kulmala, Organic condensation: A vital link connecting aerosol formation to cloud condensation nuclei (CCN) concentrations. *Atmos. Chem. Phys.* **11**, 3865–3878 (2011).
16. Y. Li, Y. Ji, J. Zhao, Y. Wang, Q. Shi, J. Peng, Y. Wang, C. Wang, F. Zhang, Y. Wang, J. H. Seinfeld, R. Zhang, Unexpected Oligomerization of Small α -Dicarbonyls for Secondary Organic Aerosol and Brown Carbon Formation. *Environ. Sci. Technol.* **55**, 4430–4439 (2021).
17. M. Shiraiwa, L. D. Yee, K. A. Schilling, C. L. Loza, J. S. Craven, A. Zuend, P. J. Ziemann, J. H. Seinfeld, Size distribution dynamics reveal particle-phase chemistry in organic aerosol formation. *Proc. Natl. Acad. Sci. U.S.A.* **110**, 11746–11750 (2013).
18. R. A. Zaveri, R. C. Easter, J. E. Shilling, J. H. Seinfeld, Modeling kinetic partitioning of secondary organic aerosol and size distribution dynamics: Representing effects of volatility, phase state, and particle-phase reaction. *Atmos. Chem. Phys.* **14**, 5153–5181 (2014).
19. T. Jokinen, T. Berndt, R. Makkonen, V. M. Kerminen, H. Junninen, P. Paasonen, F. Stratmann, H. Herrmann, A. B. Guenther, D. R. Worsnop, M. Kulmala, M. Ehn, M. Sipilä, Production of extremely low volatile organic compounds from biogenic emissions: Measured yields and atmospheric implications. *Proc. Natl. Acad. Sci.* **112**, 7123–7128 (2015).
20. J. Trostl, W. K. Chuang, H. Gordon, M. Heinritzi, C. Yan, U. Molteni, L. Ahlm, C. Frege, F. Bianchi, R. Wagner, M. Simon, K. Lehtipalo, C. Williamson, J. S. Craven, J. Duplissy, A. Adamov, J. Almeida, A.-K. Bernhammer, M. Breitenlechner, S. Brilke, A. Dias, S. Ehrhart, R. C. Flagan, A. Franchin, C. Fuchs, R. Guida, M. Gysel, A. Hansel, C. R. Hoyle, T. Jokinen, H. Junninen, J. Kangasluoma, H. Keskinen, J. Kim, M. Krapf, A. Kürten, A. Laaksonen, M. Lawler, M. Leiminger, S. Mathot, O. Möhler, T. Nieminen, A. Onnela, T. Petäjä, F. M. Piel, P. Miettinen, M. P. Rissanen, L. Rondo, N. Sarnela, S. Schobesberger, K. Sengupta, M. Sipilä, J. N. Smith, G. Steiner, A. Tomé, A. Virtanen, A. C. Wagner, E. Weingartner, D. Wimmer, P. M. Winkler, P. Ye, K. S. Carslaw, J. Curtius, J. Dommen, J. Kirkby, M. Kulmala, I. Riipinen, D. R. Worsnop, N. M. Donahue, U. Baltensperger, The role of low-volatility organic compounds in initial particle growth in the atmosphere. *Nature* **533**, 527–531 (2016).
21. R. Zhang, A. Khalizov, L. Wang, M. Hu, W. Xu, Nucleation and Growth of Nanoparticles in the Atmosphere. *Chem. Rev.* **112**, 1957–2011 (2012).
22. J. Liu, E. L. D'Ambro, B. H. Lee, F. D. Lopez-Hilfiker, R. A. Zaveri, J. C. Rivera-Rios, F. N. Keutsch, S. Iyer, T. Kurten, Z. Zhang, A. Gold, J. D. Surratt, J. E. Shilling, J. A. Thornton, Efficient isoprene secondary organic aerosol formation from a non-IEPOX pathway. *Environ. Sci. Technol.* **50**, 9872–9880 (2016).
23. E. L. D'Ambro, B. H. Lee, J. Liu, J. E. Shilling, C. J. Gaston, F. D. Lopez-Hilfiker, S. Schobesberger, R. A. Zaveri, C. Mohr, A. Lutz, Z. Zhang, A. Gold, J. D. Surratt, J. C. Rivera-Rios, F. N. Keutsch, J. A. Thornton, Molecular composition and volatility of isoprene photochemical oxidation secondary organic aerosol under low- and high-NOx conditions. *Atmos. Chem. Phys.* **17**, 159–174 (2017).
24. A. L. Robinson, N. M. Donahue, M. K. Shrivastava, E. A. Weitkamp, A. M. Sage, A. P. Grieshop, T. E. Lane, J. R. Pierce, S. N. Pandis, Rethinking organic aerosols: Semivolatile emissions and photochemical aging. *Science* **315**, 1259–1262 (2007).
25. J. F. Pankow, An absorption model of gas/particle partitioning of organic compounds in the atmosphere. *Atmos. Environ.* **28**, 185–188 (1994).
26. M. Shiraiwa, J. H. Seinfeld, Equilibration timescale of atmospheric secondary organic aerosol partitioning. *Geophys. Res. Lett.* **39**, L24801 (2012).
27. A. Virtanen, J. Joutsensaari, T. Koop, J. Kannosto, P. Yli-Pirilä, J. Leskinen, J. M. Mäkelä, J. K. Holopainen, U. Pöschl, M. Kulmala, D. R. Worsnop, A. Laaksonen, An amorphous solid state of biogenic secondary organic aerosol particles. *Nature* **467**, 824–827 (2010).
28. T. D. Vaden, D. Imre, J. Beranek, M. Shrivastava, A. Zelenyuk, Evaporation kinetics and phase of laboratory and ambient secondary organic aerosol. *Proc. Natl. Acad. Sci. U.S.A.* **108**, 2190–2195 (2011).
29. E. Saukko, A. T. Lambe, P. Massoli, T. Koop, J. P. Wright, D. R. Croasdale, D. A. Pedernera, T. B. Onasch, A. Laaksonen, P. Davidovits, D. R. Worsnop, A. Virtanen, Humidity-dependent phase state of SOA particles from biogenic and anthropogenic precursors. *Atmos. Chem. Phys.* **12**, 7517–7529 (2012).
30. L. Renbaum-Wolff, J. W. Grayson, A. P. Bateman, M. Kuwata, M. Sellier, B. J. Murray, J. E. Shilling, S. T. Martin, A. K. Bertram, Viscosity of α -pinene secondary organic material and implications for particle growth and reactivity. *Proc. Natl. Acad. Sci. U.S.A.* **110**, 8014–8019 (2013).
31. L. N. Hawkins, M. J. Baril, N. Sedehi, M. M. Galloway, D. O. de Haan, G. P. Schill, M. A. Tolbert, Formation of semisolid, oligomerized aqueous SOA: Lab simulations of cloud Processing. *Environ. Sci. Technol.* **48**, 2273–2280 (2014).
32. M. J. Song, P. Liu, S. J. Hanna, R. A. Zaveri, K. K. Potter, Y. You, S. Martin, A. K. Bertram, Relative humidity-dependent viscosity of secondary organic material from toluene photo-oxidation and possible implications for organic particulate matter over megacities. *Atmos. Chem. Phys.* **16**, 8817–8830 (2016).
33. R. A. Zaveri, J. E. Shilling, A. Zelenyuk, J. Liu, D. M. Bell, E. L. D'Ambro, C. J. Gaston, J. A. Thornton, A. Laskin, P. Lin, J. Wilson, R. C. Easter, J. Wang, A. K. Bertram, S. T. Martin, J. H. Seinfeld, D. R. Worsnop, Growth kinetics and size distribution dynamics of viscous secondary organic aerosol. *Environ. Sci. Technol.* **52**, 1191–1199 (2018).
34. R. A. Zaveri, J. E. Shilling, A. Zelenyuk, M. A. Zawadowicz, K. Suski, S. China, D. M. Bell, D. Veghte, A. Laskin, Particle-Phase Diffusion Modulates Partitioning of Semivolatile Organic Compounds to Aged Secondary Organic Aerosol. *Environ. Sci. Technol.* **54**, 2595–2605 (2020).
35. J. P. Reid, A. K. Bertram, D. O. Topping, A. Laskin, S. T. Martin, M. D. Petters, F. D. Pope, G. Rovelli, The viscosity of atmospherically relevant organic particles. *Nat. Commun.* **9**, 956 (2018).
36. A. Zelenyuk, D. G. Imre, J. Wilson, D. M. Bell, K. J. Suski, M. Shrivastava, J. Beranek, M. L. Alexander, A. L. Kramer, S. L. Massey Simonich, The effect of gas-phase polycyclic aromatic hydrocarbons on the formation and properties of biogenic secondary organic aerosol particles. *Faraday Discuss.* **200**, 143–164 (2017).
37. V. Perraud, E. A. Bruns, M. J. Ezell, S. N. Johnson, Y. Yu, M. L. Alexander, A. Zelenyuk, D. Imre, W. L. Chang, D. Dabdub, J. F. Pankow, B. J. Finlayson-Pitts, Nonequilibrium atmospheric secondary organic aerosol formation and growth. *Proc. Natl. Acad. Sci. U.S.A.* **109**, 2836–2841 (2012).
38. M. J. Apsokardu, M. V. Johnston, Nanoparticle growth by particle-phase chemistry. *Atmos. Chem. Phys.* **18**, 1895–1907 (2018).
39. Y. He, A. Akherati, T. Nah, N. L. Ng, L. A. Garofalo, D. K. Farmer, M. Shiraiwa, R. A. Zaveri, C. D. Cappa, J. R. Pierce, S. H. Jathar, Particle Size Distribution Dynamics Can Help Constrain the Phase State of Secondary Organic Aerosol. *Environ. Sci. Technol.* **55**, 1466–1476 (2021).
40. A. L. Hodshire, B. B. Palm, M. L. Alexander, Q. Bian, P. Campuzano-Jost, E. S. Cross, D. A. Day, S. S. de Sá, A. B. Guenther, A. Hansel, J. F. Hunter, W. Jud, T. Karl, S. Kim, J. H. Kroll, J. H. Park, Z. Peng, R. Seco, J. N. Smith, J. L. Jimenez, J. R. Pierce, Constraining nucleation, condensation, and chemistry in oxidation flow reactors using size-distribution measurements and aerosol microphysical modeling. *Atmos. Chem. Phys.* **18**, 12433–12460 (2018).
41. S. T. Martin, P. Artaxo, L. A. T. Machado, A. O. Manzi, R. A. F. Souza, C. Schumacher, J. Wang, M. O. Andreae, H. M. J. Barbosa, J. Fan, G. Fisch, A. H. Goldstein, A. Guenther, J. L. Jimenez, U. Pöschl, M. A. Silva Dias, J. N. Smith, M. Wendisch, Introduction: Observations and modeling of the Green Ocean Amazon (GoAmazon2014/5). *Atmos. Chem. Phys.* **16**, 4785–4797 (2016).
42. A. S. S. Medeiros, G. Calderaro, P. C. Guimaraes, M. R. Magalhaes, M. V. B. Morais, S. A. A. Rafee, I. O. Ribeiro, R. V. Andreoli, J. A. Martins, L. D. Martins, S. T. Martin, R. A. F. Souza, Power plant fuel switching and air quality in a tropical, forested environment. *Atmos. Chem. Phys.* **17**, 8987–8998 (2017).
43. G. Cirino, J. Brito, H. M. J. Barbosa, L. V. Rizzo, P. Tunved, S. S. de Sá, J. L. Jimenez, B. B. Palm, S. Carbone, J. V. Lavric, R. A. F. Souza, S. Wolff, D. Walter, J. Tota, M. B. L. Oliveira, S. T. Martin, P. Artaxo, Observations of Manaus urban plume evolution and interaction with biogenic emissions in GoAmazon 2014/5. *Atmos. Environ.* **191**, 513–524 (2018).
44. J. E. Shilling, M. S. Pekour, E. C. Fortner, P. Artaxo, S. de Sá, J. M. Hubbe, K. M. Longo, L. A. T. Machado, S. T. Martin, S. R. Springston, J. Tomlinson, J. Wang, Aircraft observations of the chemical composition and aging of aerosol in the Manaus urban plume during GoAmazon 2014/5. *Atmos. Chem. Phys.* **18**, 10773–10797 (2018).
45. B. Zhao, J. D. Fast, N. M. Donahue, M. Shrivastava, M. Schervish, J. E. Shilling, H. Gordon, J. Wang, Y. Gao, R. A. Zaveri, Y. Liu, B. Gaudet, Impact of Urban Pollution on Organic-Mediated New-Particle Formation and Particle Number Concentration in the Amazon Rainforest. *Environ. Sci. Technol.* **55**, 4357–4367 (2021).
46. U. Pöschl, S. T. Martin, B. Sinha, Q. Chen, S. S. Gunthe, J. A. Huffman, S. Borrmann, D. K. Farmer, R. M. Garland, G. Helas, J. L. Jimenez, S. M. King, A. Manzi, E. Mikhailov, T. Pauliquevis, M. D. Petters, A. J. Prenni, P. Roldin, D. Rose, J. Schneider, H. Su, S. R. Zorn, P. Artaxo, M. O. Andreae, Rainforest Aerosols as Biogenic Nuclei of Clouds and Precipitation in the Amazon. *Science* **329**, 1513–1516 (2010).
47. D. Gu, A. B. Guenther, J. E. Shilling, H. Yu, M. Huang, C. Zhao, Q. Yang, S. T. Martin, P. Artaxo, S. Kim, R. Seco, T. Stavrou, K. M. Longo, J. Tóta, R. A. F. de Souza, O. Vega, Y. Liu, M. Shrivastava, E. G. Alves, F. C. Santos, G. Leng, Z. Hu, Airborne observations reveal elevational gradient in tropical forest isoprene emissions. *Nat. Commun.* **8**, 15541 (2017).
48. S. T. Martin, P. Artaxo, L. Machado, A. O. Manzi, R. A. F. Souza, C. Schumacher, J. Wang, T. Biscaro, J. Brito, A. Calheiros, K. Jardine, A. Medeiros, B. Portela, S. S. de Sá, K. Adachi, A. C. Aiken, R. Albrecht, L. Alexander, M. O. Andreae, H. M. J. Barbosa, P. Buseck, D. Chand, J. M. Comstock, D. A. Day, M. Dubey, J. Fan, J. Fast, G. Fisch, E. Fortner, S. Giangrande, M. Gilles, A. H. Goldstein, A. Guenther, J. Hubbe, M. Jensen, J. L. Jimenez, F. N. Keutsch, S. Kim, C. Kuang, A. Laskin, K. McKinney, F. Mei, M. Miller, R. Nascimento, T. Pauliquevis, M. Pekour, J. Peres, T. Petäjä, C. Pöhlker, U. Pöschl, L. Rizzo, B. Schmid, J. E. Shilling, M. A. S. Dias, J. N. Smith, J. M. Tomlinson, J. Tóta, M. Wendisch, The Green Ocean Amazon Experiment (Goamazon2014/5) Observes Pollution Affecting Gases, Aerosols, Clouds, and Rainfall over the Rain Forest. *Bull. Am. Meteorol. Soc.* **98**, 981–997 (2017).

49. J. W. Fan, D. Rosenfeld, Y. Zhang, S. E. Giangrande, Z. Li, L. A. T. Machado, S. T. Martin, Y. Yang, J. Wang, P. Artaxo, H. M. J. Barbosa, R. C. Braga, J. M. Comstock, Z. Feng, W. Gao, H. B. Gomes, F. Mei, C. Pöhlker, M. L. Pöhlker, U. Pöschl, R. A. F. de Souza, Substantial convection and precipitation enhancements by ultrafine aerosol particles. *Science* **359**, 411–418 (2018).
50. M. Shrivastava, M. O. Andreae, P. Artaxo, H. M. J. Barbosa, L. K. Berg, J. Brito, J. Ching, R. C. Easter, J. Fan, J. D. Fast, Z. Feng, J. D. Fuentes, M. Glasius, A. H. Goldstein, E. G. Alves, H. G. Gomes, D. Gu, A. Guenther, S. H. Jathar, S. Kim, Y. Liu, S. Lou, S. T. Martin, V. F. McNeill, A. Medeiros, S. S. de Sá, J. E. Shilling, S. R. Springston, R. A. F. Souza, J. A. Thornton, G. Isaacman-VanWertz, L. D. Yee, R. Ynoue, R. A. Zaveri, A. Zelenyuk, C. Zhao, Urban pollution greatly enhances formation of natural aerosols over the Amazon rainforest. *Nat. Commun.* **10**, 1046 (2019).
51. L. D. Yee, G. Isaacman-VanWertz, R. A. Wernis, M. Meng, V. Rivera, N. M. Kreisberg, S. V. Hering, M. S. Bering, M. Glasius, M. A. Upshur, A. Gray Bé, R. J. Thomson, F. M. Geiger, J. H. Offenberg, M. Lewandowski, I. Kourtchev, M. Kalberer, S. de Sá, S. T. Martin, J. M. Alexander, B. B. Palm, W. Hu, P. Campuzano-Jost, D. A. Day, J. L. Jimenez, Y. Liu, K. A. McKinney, P. Artaxo, J. Viegas, A. Manzi, M. B. Oliveira, R. de Souza, L. A. T. Machado, K. Longo, A. H. Goldstein, Observations of sesquiterpenes and their oxidation products in central Amazonia during the wet and dry seasons. *Atmos. Chem. Phys.* **18**, 10433–10457 (2018).
52. Y. H. Lin, Z. Zhang, K. S. Docherty, H. Zhang, S. H. Budisulistiorini, C. L. Rubitschun, S. L. Shaw, E. M. Knipping, E. S. Edgerton, T. E. Kleindienst, A. Gold, J. D. Surratt, Isoprene epoxydiols as precursors to secondary organic aerosol formation: Acid-catalyzed reactive uptake studies with authentic compounds. *Environ. Sci. Technol.* **46**, 250–258 (2012).
53. J. D. Surratt, A. W. H. Chan, N. C. Eddingsaas, M. Chan, C. L. Loza, A. J. Kwan, S. P. Hersey, R. C. Flagan, P. O. Wennberg, J. H. Seinfeld, Reactive intermediates revealed in secondary organic aerosol formation from isoprene. *Proc. Natl. Acad. Sci. U.S.A.* **107**, 6640–6645 (2010).
54. S. S. de Sá, B. B. Palm, P. Campuzano-Jost, D. A. Day, M. K. Newburn, W. Hu, G. Isaacman-VanWertz, L. D. Yee, R. Thalman, J. Brito, S. Carbone, P. Artaxo, A. H. Goldstein, A. O. Manzi, R. A. F. Souza, F. Mei, J. E. Shilling, S. R. Springston, J. Wang, J. D. Surratt, M. L. Alexander, J. L. Jimenez, S. T. Martin, Influence of urban pollution on the production of organic particulate matter from isoprene epoxydiols in central Amazonia. *Atmos. Chem. Phys.* **17**, 6611–6629 (2017).
55. J. E. Krechmer, M. M. Coggon, P. Massoli, T. B. Nguyen, J. D. Crouse, W. Hu, D. A. Day, G. S. Tyndall, D. K. Henze, J. C. Rivera-Rios, J. B. Nowak, J. R. Kimmel, R. L. Mauldin III, H. Stark, J. T. Jayne, M. Sipilä, H. Junninen, J. M. St. Clair, X. Zhang, P. A. Feiner, L. Zhang, D. O. Miller, W. H. Brune, F. N. Keutsch, P. O. Wennberg, J. H. Seinfeld, D. R. Worsnop, J. L. Jimenez, M. R. Canagaratna, Formation of low volatility organic compounds and secondary organic aerosol from isoprene hydroxyhydroperoxide low-NO oxidation. *Environ. Sci. Technol.* **49**, 10330–10339 (2015).
56. A. P. Bateman, Z. Gong, P. Liu, B. Sato, G. Cirino, Y. Zhang, P. Artaxo, A. K. Bertram, A. O. Manzi, L. V. Rizzo, R. A. F. Souza, R. A. Zaveri, S. T. Martin, Sub-micrometre particulate matter is primarily in liquid form over Amazon rainforest. *Nat. Geosci.* **9**, 34–37 (2016).
57. A. P. Bateman, Z. Gong, T. H. Harder, S. S. de Sá, B. Wang, P. Castillo, S. China, Y. Liu, R. E. O'Brien, B. B. Palm, H. W. Shiu, G. G. Cirino, R. Thalman, K. Adachi, M. L. Alexander, P. Artaxo, A. K. Bertram, P. R. Buseck, M. K. Gilles, J. L. Jimenez, A. Laskin, A. O. Manzi, A. Sedlacek, R. A. F. Souza, J. Wang, R. Zaveri, S. T. Martin, Anthropogenic influences on the physical state of submicron particulate matter over a tropical forest. *Atmos. Chem. Phys.* **17**, 1759–1773 (2017).
58. R. A. Zaveri, R. C. Easter, J. D. Fast, L. K. Peters, Model for Simulating Aerosol Interactions and Chemistry (MOSAIC). *J. Geophys. Res.-Atmos.* **113**, D13204 (2008).
59. M. L. Smith, A. K. Bertram, S. T. Martin, Deliquescence, efflorescence, and phase miscibility of mixed particles of ammonium sulfate and isoprene-derived secondary organic material. *Atmos. Chem. Phys.* **12**, 9613–9628 (2012).
60. C. M. Wu, B. Stevens, A. Arakawa, What Controls the Transition from Shallow to Deep Convection? *J. Atmos. Sci.* **66**, 1793–1806 (2009).
61. W.-K. Tao, J.-P. Chen, Z. Li, C. Wang, C. Zhang, Impact of aerosols on convective clouds and precipitation. *Rev. Geophys.* **50**, (2012).
62. M. A. Cecchini, L. A. T. Machado, J. M. Comstock, F. Mei, J. Wang, J. Fan, J. M. Tomlinson, B. Schmid, R. Albrecht, S. T. Martin, P. Artaxo, Impacts of the Manaus pollution plume on the microphysical properties of Amazonian warm-phase clouds in the wet season. *Atmos. Chem. Phys.* **16**, 7029–7041 (2016).
63. A. Cheng, K.-M. Xu, Simulation of Boundary-Layer Cumulus and Stratocumulus Clouds Using a Cloud-Resolving Model with Low-and Third-order Turbulence Closures. *J. Meteorol. Soc. Japan* **86A**, 67–86 (2008).
64. S.-L. Tai, J. D. Fast, W. I. Gustafson Jr., D. Chand, B. Gaudet, Z. Feng, R. Newsom, Simulation of Continental Shallow Cumulus Populations Using an Observation-Constrained Cloud-System Resolving Model. *J. Adv. Model. Earth Syst.* **12**, e2020MS002091 (2020).
65. C. E. Scott, D. V. Spracklen, J. R. Pierce, I. Riipinen, S. D. D'Andrea, A. Rap, K. S. Carslaw, P. M. Forster, P. Artaxo, M. Kulmala, L. V. Rizzo, E. Swietlicki, G. W. Mann, K. J. Pringle, Impact of gas-to-particle partitioning approaches on the simulated radiative effects of biogenic secondary organic aerosol. *Atmos. Chem. Phys.* **15**, 12989–13001 (2015).
66. M. Shiraiwa, Y. Li, A. P. Tsimpidi, V. A. Karydis, T. Berkemeier, S. N. Pandis, J. Lelieveld, T. Koop, U. Pöschl, Global distribution of particle phase state in atmospheric secondary organic aerosols. *Nat. Commun.* **8**, 15002 (2017).
67. B. Schmid, J. M. Tomlinson, J. M. Hubbe, J. M. Comstock, F. Mei, D. Chand, M. S. Pekour, C. D. Kluzek, E. Andrews, S. C. Biraud, G. M. McFarquhar, The DOE ARM Aerial Facility. *Bull. Am. Meteorol. Soc.* **95**, 723–742 (2014).
68. L. I. Kleinman, P. H. Daum, Y.-N. Lee, G. I. Senum, S. R. Springston, J. Wang, C. Berkowitz, J. Hubbe, R. A. Zaveri, F. J. Brechtel, J. Jayne, T. B. Onasch, D. Worsnop, Aircraft observations of aerosol composition and ageing in New England and Mid-Atlantic States during the summer 2002 New England Air Quality Study field campaign. *J. Geophys. Res.-Atmos.* **112**, D09310 (2007).
69. G. J. Sem, Design and performance characteristics of three continuous-flow condensation particle counters: A summary. *Atmos. Res.* **62**, 267–294 (2002).
70. J. S. Olfert, P. Kulkarni, J. Wang, Measuring aerosol size distributions with the fast integrated mobility spectrometer. *J. Aerosol Sci.* **39**, 940–956 (2008).
71. J. Wang, M. Pikridas, S. R. Spielman, T. Pinterich, A fast integrated mobility spectrometer for rapid measurement of sub-micrometer aerosol size distribution, Part I: Design and model evaluation. *J. Aerosol Sci.* **108**, 44–55 (2017).
72. S. Lance, A. Nenes, J. Medina, J. N. Smith, Mapping the Operation of the DMT Continuous Flow CCN Counter. *Aerosol Sci. Tech.* **40**, 242–254 (2006).
73. P. F. DeCarlo, J. R. Kimmel, A. Trimborn, M. J. Northway, J. T. Jayne, A. C. Aiken, M. Gonin, K. Fuhrer, T. Horvath, K. S. Docherty, D. R. Worsnop, J. L. Jimenez, Field-deployable, high-resolution, time-of-flight aerosol mass spectrometer. *Anal. Chem.* **78**, 8281–8289 (2006).
74. M. R. Canagaratna, J. L. Jimenez, J. H. Kroll, Q. Chen, S. H. Kessler, P. Massoli, L. Hildebrandt Ruiz, E. Fortner, L. R. Williams, K. R. Wilson, J. D. Surratt, N. M. Donahue, J. T. Jayne, D. R. Worsnop, Elemental ratio measurements of organic compounds using aerosol mass spectrometry: Characterization, improved calibration, and implications. *Atmos. Chem. Phys.* **15**, 253–272 (2015).
75. W. Lindinger, A. Hansel, A. Jordan, On-line monitoring of volatile organic compounds at pptv levels by means of proton-transfer-reaction mass spectrometry (PTR-MS) - Medical applications, food control and environmental research. *Int. J. Mass Spectrom.* **173**, 191–241 (1998).
76. D. Baumgardner, S. J. Abel, D. Axisa, R. Cotton, J. Crosier, P. Field, C. Gurganus, A. Heymsfield, A. Korolev, M. Krämer, P. Lawson, G. McFarquhar, Z. Ulanowski, J. Um, Cloud Ice Properties: In Situ Measurement Challenges. *Meteorol. Monogr.* **58**, 9.1–9.23 (2017).
77. D. H. Lenschow, V. Wulfmeyer, C. Senff, Measuring second- through fourth-order moments in noisy data. *J. Atmos. Oceanic Tech.* **17**, 1330–1347 (2000).
78. L. K. Berg, R. K. Newsom, D. D. Turner, Year-Long Vertical Velocity Statistics Derived from Doppler Lidar Data for the Continental Convective Boundary Layer. *J. Appl. Meteorol. Climatol.* **56**, 2441–2454 (2017).
79. N. Rastak, A. Pajunoja, J. C. Acosta Navarro, J. Ma, M. Song, D. G. Partridge, A. Kirkevåg, Y. Leong, W. W. Hu, N. F. Taylor, A. Lambe, K. Cerully, A. Bougiatioti, P. Liu, R. Krejci, T. Petäjä, C. Percival, P. Davidovits, D. R. Worsnop, A. M. L. Ekman, A. Nenes, S. Martin, J. L. Jimenez, D. R. Collins, D. O. Topping, A. K. Bertram, A. Zuend, A. Virtanen, I. Riipinen, Microphysical explanation of the RH-dependent water affinity of biogenic organic aerosol and its importance for climate. *Geophys. Res. Lett.* **44**, 5167–5177 (2017).
80. C. Schumacher, A. Funk, GoAmazon2014/5 three-dimensional gridded S-band reflectivity and radial velocity from the SIPAM Manaus S-band radar (United States: N. p., 2018); doi:10.5439/1459573.

Acknowledgments: We thank the G-1 flight and ground crews for supporting the GoAmazon2014/5 mission. We are grateful to K. M. Longo for the leadership related to the G-1 aircraft as part of GoAmazon2014/5. We gratefully acknowledge S. R. Springston (Brookhaven National Laboratory) for the NO_y data on the G-1, S. Kim (University of California, Irvine) for the OH radical data at the T3 ground site, and C. Schumacher and A. Funk (Texas A&M University) for the SIPAM S-band radar data. **Funding:** Funding for data collection onboard the G-1 aircraft and at the ground sites was provided by the Atmospheric Radiation Measurement (ARM) Climate Research Facility, a U.S. Department of Energy (DOE) Office of Science user facility sponsored by the Office of Biological and Environmental Research (OBER). We also acknowledge the support provided by the Environmental Molecular Sciences Laboratory (EMSL), a national scientific user facility sponsored by the OBER at Pacific Northwest National Laboratory (PNNL). The S-band (SIPAM) radar data were supported by the CHUVA project. Data analysis and research were supported by the U.S. DOE's Atmospheric System Research Program under contract DE-AC06-76RLO 1830 at PNNL and contract DE-SC0020259 for J.W. Effort of J.F. and Y.Z. was supported by the DOE Early Career Research Program. PNNL is operated for the U.S. DOE by Battelle Memorial Institute. We acknowledge

the support from the Central Office of the Large Scale Biosphere Atmosphere Experiment in Amazonia (LBA), the Instituto Nacional de Pesquisas da Amazonia (INPA), and the Instituto Nacional de Pesquisas Espaciais (INPE). Paulo Artaxo acknowledges Fundação de Amparo à Pesquisa do Estado de São Paulo (FAPESP) grants 2013/05014-0 and 2017/17047-0. The work was conducted under licenses 001262/2012-2 and 001030/2012-4 of the Brazilian National Council for Scientific and Technological Development (CNPq). **Author contributions:** R.A.Z., J.W., J.F., J.E.S., and S.T.M. designed the research. R.A.Z., J.W., J.F., Y.Z., J.E.S., F.M., and R.N. performed research. J.W., Y.Z., J.E.S., F.M., R.N., M.P., J.T., J.M.C., and E.F. processed data and performed analyses. R.A.Z. performed aerosol modeling. Y.Z. and J.F. performed cloud modeling. A.Z. contributed to data interpretation. M.S. contributed to modeling. R.A.Z., J.W., J.F., Y.Z., J.E.S., A.Z., F.M., R.N., M.P., L.A.T.M., P.A., and S.T.M. wrote the manuscript, with inputs from all coauthors. **Competing interests:** The authors declare that they have no

competing interests. **Data and materials availability:** All data needed to evaluate the conclusions in the paper are present in the paper and/or the Supplementary Materials. GoAmazon2014/5 field campaign data used in this study are publicly available on the DOE's ARM website: <http://campaign.arm.gov/goamazon2014/observations/>. The Terra Moderate Resolution Imaging Spectroradiometer (MODIS) collection 6.1° (C61) level-2 cloud retrieval products (MOD06_L2) with 1-km resolution are used for the observed cloud water path are available at dx.doi.org/10.5067/MODIS/MOD06_L2.006.

Submitted 16 April 2021

Accepted 18 November 2021

Published 12 January 2022

10.1126/sciadv.abj0329

Rapid growth of anthropogenic organic nanoparticles greatly alters cloud life cycle in the Amazon rainforest

Rahul A. ZaveriJian WangJiwen FanYuwei ZhangJohn E. ShillingAlla ZelenyukFan MeiRob NewsomMikhail PekourJason TomlinsonJennifer M. ComstockManish ShrivastavaEdward FortnerLuiz A. T. MachadoPaulo ArtaxoScot T. Martin

Sci. Adv., 8 (2), eabj0329. • DOI: 10.1126/sciadv.abj0329

View the article online

<https://www.science.org/doi/10.1126/sciadv.abj0329>

Permissions

<https://www.science.org/help/reprints-and-permissions>

Use of think article is subject to the [Terms of service](#)

Science Advances (ISSN) is published by the American Association for the Advancement of Science. 1200 New York Avenue NW, Washington, DC 20005. The title *Science Advances* is a registered trademark of AAAS.
Copyright © 2022 The Authors, some rights reserved; exclusive licensee American Association for the Advancement of Science. No claim to original U.S. Government Works. Distributed under a Creative Commons Attribution NonCommercial License 4.0 (CC BY-NC).